

LetsGo: Large-Scale Garage Modeling and Rendering via LiDAR-Assisted Gaussian Primitives

JIADI CUI*, ShanghaiTech University, China and Stereye Intelligent Technology Co.,Ltd., China

JUNMING CAO*, Shanghai Advanced Research Institute, Chinese Academy of Sciences, China and University of Chinese Academy of Sciences, China

FUQIANG ZHAO*, ShanghaiTech University, China and NeuDim Digital Technology (Shanghai) Co.,Ltd., China

ZHIPENG HE, ShanghaiTech University, China

YIFAN CHEN, ShanghaiTech University, China

YUHUI ZHONG, DGene Digital Technology Co., Ltd., China

LAN XU, ShanghaiTech University, China

YUJIAO SHI[†], ShanghaiTech University, China

YINGLIANG ZHANG[†], DGene Digital Technology Co., Ltd., China

JINGYI YU[†], ShanghaiTech University, China

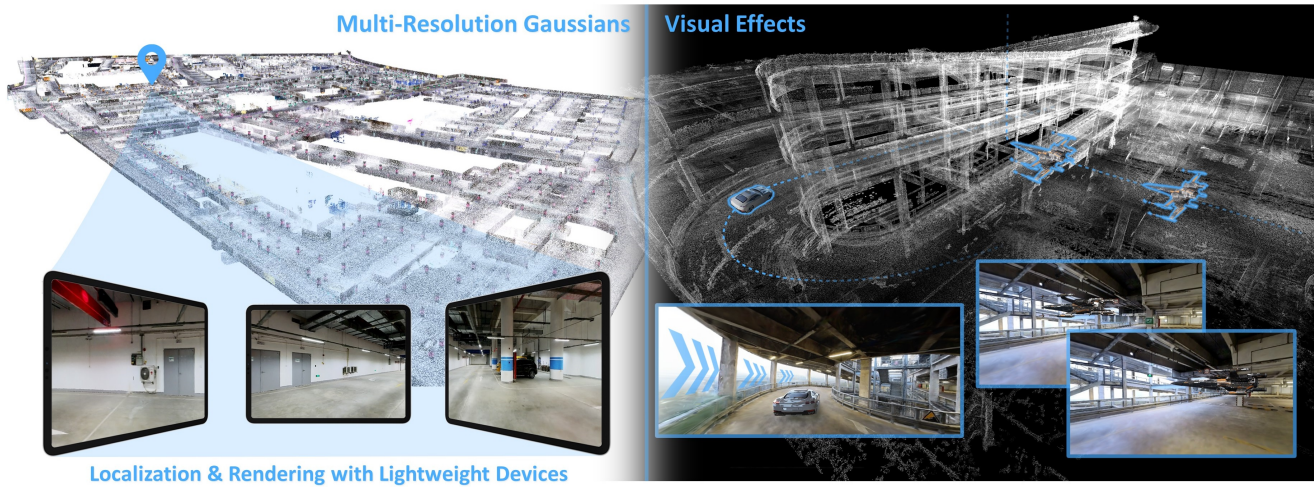


Fig. 1. We present LetsGo - an explicit and efficient end-to-end framework for high-fidelity rendering of large-scale garages. We design a handheld Polar scanner to capture RGBD data of expansive parking environments and have scanned a garage dataset, named GarageWorld, comprising eight garages with different structures. Our LiDAR-assisted Gaussian primitives approach along with GarageWorld dataset enables various applications, such as autonomous vehicle localization, navigation and parking, as well as VFX production.

*Equal contributions.

[†]Corresponding author.

Authors' addresses: Jiadi Cui, ShanghaiTech University, Shanghai, China and Stereye Intelligent Technology Co.,Ltd., China, cuijd@shanghaitech.edu.cn; Junming Cao, Shanghai Advanced Research Institute, Chinese Academy of Sciences, Shanghai, China and University of Chinese Academy of Sciences, Beijing, China, caojm@sari.ac.cn; Fuqiang Zhao, ShanghaiTech University, Shanghai, China and NeuDim Digital Technology (Shanghai) Co.,Ltd., China, zhaofq@shanghaitech.edu.cn; Zhipeng He, ShanghaiTech University, Shanghai, China, hezhp2023@shanghaitech.edu.cn; Yifan Chen, ShanghaiTech University, Shanghai, China, chenyf2022@shanghaitech.edu.cn; Yuhui Zhong, DGene Digital Technology Co., Ltd., China, yuhui.zhong@dgene.com; Lan Xu, ShanghaiTech University, Shanghai, China, xulan1@shanghaitech.edu.cn; Yujiao Shi, ShanghaiTech University, Shanghai, China, syujiao93@gmail.com; Yingliang Zhang, DGene Digital Technology Co., Ltd., China, yingliang.dgene@gmail.com; Jingyi Yu, ShanghaiTech University, Shanghai, China, yujingyi@shanghaitech.edu.cn.

Permission to make digital or hard copies of part or all of this work for personal or classroom use is granted without fee provided that copies are not made or distributed for profit or commercial advantage and that copies bear this notice and the full citation

Large garages are ubiquitous yet intricate scenes that present unique challenges due to their monotonous colors, repetitive patterns, reflective surfaces, and transparent vehicle glass. Conventional Structure from Motion (SfM) methods for camera pose estimation and 3D reconstruction often fail in these environments due to poor correspondence construction. To address these challenges, we introduce LetsGo, a LiDAR-assisted Gaussian splatting framework for large-scale garage modeling and rendering. We develop a handheld scanner, Polar, equipped with IMU, LiDAR, and a fisheye camera, to facilitate accurate data acquisition. Using this Polar device, we present the GarageWorld dataset, consisting of eight expansive garage scenes with

on the first page. Copyrights for third-party components of this work must be honored. For all other uses, contact the owner/author(s).

© 2024 Copyright held by the owner/author(s).

0730-0301/2024/12-ART

<https://doi.org/10.1145/3687762>

diverse geometric structures, which will be made publicly available for further research. Our approach demonstrates that LiDAR point clouds collected by the Polar device significantly enhance a suite of 3D Gaussian splatting algorithms for garage scene modeling and rendering. We introduce a novel depth regularizer that effectively eliminates floating artifacts in rendered images. Additionally, we propose a multi-resolution 3D Gaussian representation designed for Level-of-Detail (LOD) rendering. This includes adapted scaling factors for individual levels and a random-resolution-level training scheme to optimize the Gaussians across different resolutions. This representation enables efficient rendering of large-scale garage scenes on lightweight devices via a web-based renderer. Experimental results on our GarageWorld dataset, as well as on ScanNet++ and KITTI-360, demonstrate the superiority of our method in terms of rendering quality and resource efficiency.

CCS Concepts: • **Computing methodologies** → **Computational photography; Image-based rendering.**

Additional Key Words and Phrases: Neural rendering, large-scale garage modeling, LiDAR scanning, 3D Gaussian splatting, garage dataset, level-of-detail rendering

ACM Reference Format:

Jiadi Cui, Junming Cao, Fuqiang Zhao, Zhipeng He, Yifan Chen, Yuhui Zhong, Lan Xu, Yujiao Shi, Yingliang Zhang, and Jingyi Yu. 2024. LetsGo: Large-Scale Garage Modeling and Rendering via LiDAR-Assisted Gaussian Primitives. *ACM Trans. Graph.* 43, 6 (December 2024), 18 pages. <https://doi.org/10.1145/3687762>

1 INTRODUCTION

Modeling garage environments accurately is crucial for various applications such as autonomous vehicle testing, architectural planning, and game design. Garages present a unique set of challenges due to their complex geometries, varying lighting conditions, and frequent presence of obstacles. The ability to create detailed and realistic 3D models of garages can significantly enhance the effectiveness of these applications, providing more accurate simulations and analyses. For visual artists, garages represent a frontier in visual simulation that merges the aesthetic with the technical, offering a canvas where the intricacies of light, shadow, texture, and space coalesce. The complex interplay of artificial and natural lighting within the confines of a garage, with its reflective surfaces, varying materials, and intricate geometries, provides a rigorous testbed for modeling and rendering, pushing the boundaries of what is achievable in virtual environments.

However, capturing and rendering garage environments poses significant difficulties. These spaces often have low-light conditions, textureless surfaces, and a high degree of clutter (Fig. 4). The intricacies of garage layouts, including narrow spaces and reflective surfaces, further complicate the modeling process. Garages with internal circular or spiral paths often lead to incomplete data and ambiguities in spatial relationships. Additionally, their extensive spatial area underscores the necessity for efficient 3D representations and lightweight rendering techniques to facilitate real-time interaction and visualization, particularly for scenarios demanding rapid situational assessment, such as navigation and path adjustment.

Existing methods for garage modeling typically rely on either manual measurements or conventional photogrammetry and LiDAR scanning. Traditional computer vision techniques, such as Structure from Motion (SfM) [Schönberger and Frahm 2016; Snavely et al. 2008] and Multi-view Stereo (MVS) [Furukawa and Ponce 2010;

Yao et al. 2018], often struggle in these environments due to the prevalence of texture-less regions and repetitive structural designs. These methods frequently fail to extract sufficient feature points and establish accurate feature correspondences necessary for estimating camera poses. Active sensing technologies based on LiDAR can calculate camera poses and scene geometry using SLAM algorithms, but the reflective materials and transparent car windows common in garages lead to geometric inaccuracies. Moreover, LiDAR data tend to be sparse, containing many holes that corrupt high-frequency textures essential for rendering the color appearance of the scene.

While recent advances in neural representation, particularly Neural Radiance Fields (NeRF) [Mildenhall et al. 2021], have shown promise in producing high-quality renderings, they come with high computational costs and lengthy training times. Although enhancements [Deng et al. 2022; Sun et al. 2022; Xu et al. 2022; Zhang et al. 2020] to NeRF aim to optimize training duration and visual rendering quality, integrating such implicit representations into conventional graphics rendering pipelines and tools for rapid 3D content applications remains challenging. The emerging 3D Gaussian Splatting (3DGS) [Kerbl et al. 2023] method revisits explicit representations, using 3D Gaussians to articulate the geometry and appearance of scenes, achieving high-quality scene modeling and rendering. Recent works [Kerbl et al. 2024; Liu et al. 2024; Lu and Dai. 2024; Ren et al. 2024; Shuai et al. 2024] extend the 3DGS approach to model large-scale outdoor scenes, achieving impressive results. However, few methods address the unique challenges of modeling large-scale indoor scenes like underground garages, where low lighting, large texture-less regions, and repetitive patterns complicate the establishment of sufficient feature correspondences between different images.

This paper introduces LetsGo, an explicit and efficient end-to-end modeling scheme for high-fidelity rendering of large-scale garages. Our key innovation is the integration of calibrated LiDAR points into 3D Gaussian splatting algorithms. We design a handheld Polar scanner, which combines IMU, LiDAR, and a fisheye camera for robust relative pose estimation, specifically tailored for expansive garage data collection. We scan eight large-scale garages, collectively named GarageWorld, using this Polar scanner. To our knowledge, this dataset is the first of its kind aimed at large-scale garages and will be made available to the community. Our experiments demonstrate that LiDAR points collected by the Polar device effectively support various Gaussian splatting algorithms for detailed garage scene representation. To enhance the quality of 3D Gaussian rendering, we introduce a depth regularizer that uses depth priors as supervisory signals, significantly reducing floating artifacts and enabling high rendering quality.

As the scene size increases, the memory demands for rendering large amounts of 3D Gaussians can exceed the capabilities of even high-end GPUs. To address this challenge, we propose a multi-resolution 3D Gaussian representation tailored for Level-of-Detail (LOD) rendering. This approach dynamically adjusts based on the camera's position, orientation, and viewing frustum, allowing for real-time, high-quality rendering of expansive scenes. Specifically, we construct different levels of Gaussians at varying resolutions, where lower-resolution levels capture coarse scene characteristics and higher-resolution levels reconstruct fine, high-frequency details.

We employ tailored scaling factors for each level and a random-resolution-level training scheme to optimize the Gaussians across different levels.

During rendering, we introduce a novel level selection strategy that optimizes the trade-off between visual fidelity and device performance by considering the distance between 3D Gaussians and the rendering viewpoint. With our multi-resolution 3D Gaussian framework, we develop an LOD PC viewer that achieves rendering speeds up to four times faster than traditional 3DGS viewers on high-performance GPUs (e.g., RTX 3090). Additionally, we offer a lightweight web renderer designed to support LOD rendering across various consumer-level devices, including laptops and tablets. We have released our source codes, including our training code, high-performance PC viewer, and lightweight web viewer, to facilitate reproducible research. Please refer to our [project page](#).

Our results, gathered from the GarageWorld dataset as well as ScanNet++ [Dai et al. 2017] and KITTI-360 [Liao et al. 2022] datasets, indicate that our approach not only surpasses other methods in rendering quality but also maintains high rendering efficiency. The GarageWorld dataset and the LetsGo framework for large-scale garage modeling and rendering enable various applications, including autonomous driving, localization, navigation, visual effects, etc.

2 RELATED WORK

Conventional Explicit Visual Reconstruction. Conventional algorithms for reconstructing large-scale scenes include Structure from Motion (SfM) [Moulon et al. 2013; Sweeney et al. 2016; Wu 2013], Simultaneous Localization and Mapping (SLAM) [Bavle et al. 2023; Bujanca et al. 2021; Ceriani et al. 2015; Leonard and Durrant-Whyte 1991] and Multi-View Stereo (MVS) [Furukawa et al. 2010; Goele et al. 2007; Seitz et al. 2006]. They are dedicated to discerning the three-dimensional structure of a scene through the sequential or multi-view analysis of two-dimensional image frames. All these methods leverage feature tracking and multi-view consistency to recover the 3D scene structures. SfM- and SLAM-based methods [Agarwal et al. 2011; Crandall et al. 2011; Frahm et al. 2010; Heinly et al. 2015; Li et al. 2020; Schmuck et al. 2021; Teed and Deng 2021] estimate poses of input images and recover the scene structure jointly. However, their main purpose is pose estimation, and the recovered scene point clouds are always sparse, making it difficult for high-quality free-view synthesis. While MVS-based methods [Dai et al. 2019; Huang et al. 2021; Li et al. 2022; Xu et al. 2021a,b; Yang et al. 2021], especially depth-based approaches, compute a dense depth map for each input image, the constructed scenes often lack accuracy and robustness in texture-less and complex scenes.

NeRF and 3D Gaussian Splatting Variants. Recent advances [Chen et al. 2021; Kerr et al. 2023; Noguchi et al. 2021; Rebain et al. 2021; Yu et al. 2021; Zhao et al. 2022a,b] in neural scene representation have significantly impacted novel view synthesis. Neural Radiance Fields (NeRF), introduced by Mildenhall et al. [2021], have revolutionized 3D reconstruction with a novel framework for detailed scene capture. Subsequent improvements [Kulhanek and Sattler 2023; Rematas et al. 2022; Roessle et al. 2022; Sun et al. 2023] have aimed at enhancing the visual fidelity and computational efficiency of NeRF. MipNeRF [Barron et al. 2021] and MipNeRF360 [Barron et al. 2022]

address aliasing via a novel conical frustum rendering technique and a nonlinear scene representation, respectively. Techniques such as Plexvoxels [Fridovich-Keil et al. 2022], Instant-NGP [Müller et al. 2022], and TensoRF [Chen et al. 2022] have expedited rendering by integrating explicit encoding methods with compact MLP networks. Furthermore, Block-NeRF [Tancik et al. 2022] and Mega-NeRF [Turki et al. 2022] facilitate the application of NeRF to extensive scenes. F2-NeRF [Wang et al. 2023] introduces a space-warping method for handling arbitrary camera trajectories. ScaNeRF [Wu et al. 2023] optimizes camera pose and scene representation jointly to address pose drift in large-scale scene reconstruction. Unlike these NeRF-based approaches, our method employs an explicit 3D Gaussian representation with depth priors from our RGBD scanner, enhancing realism and efficiency.

3D Gaussian Splatting (3DGS) [Kerbl et al. 2023] is a transformative approach characterized by its efficiency and lifelike visual quality. Extensive research [Charatan et al. 2024; Jiang et al. 2024; Keetha et al. 2024; Lu and Dai. 2024; Matsuki et al. 2024; Niedermayr et al. 2024; Tang et al. 2023; Wu et al. 2024] has built on 3DGS. Mip-Splatting [Yu et al. 2024] mitigates artifacts from varying view sampling rates, and GaussianPro [Cheng et al. 2024], which enhances Gaussian distribution with 2D image constraints. DN-Splatter [Turkulainen et al. 2024] and DNGaussian [Li et al. 2024] use depth and normal cues for refinement. SuGaR [Guédon and Lepetit 2024] introduces Gaussian alignment regularization for explicit mesh extraction, and GaussianSurfels [Dai et al. 2024] flattens 3D Gaussian ellipsoids into 2D ellipses for accurate surface reconstructions. 2DGS [Huang et al. 2024] transforms 3D volumes into 2D planar Gaussian disks, employing a perspective-accurate 2D splatting process aligned with geometric surfaces.

TRIPS [Franke et al. 2024] combines the strengths of 3D Gaussian Splatting and advanced point-based rendering [Aliev et al. 2020; Kopanas et al. 2021] by employing the concept of rasterizing points into a screen-space image pyramid, enabling high-quality reconstruction and rendering of complex details. Despite these advances focusing on small-scale or object-level scenes, our approach innovates with a depth regularizer and a multi-resolution Gaussian representation designed for large-scale scenes, achieving realistic visual quality and enhanced rendering efficiency.

Gaussian Splatting for Large-Scale Scenes. To effectively manage large-scale scenes, VastGaussian [Lin et al. 2024] explores various partitioning strategies and introduces an appearance embedding module to enhance Gaussian training. Concurrent works such as DrivingGaussian [Zhou et al. 2024] and Street Gaussian [Yan et al. 2024] adapt Gaussian methodologies to the dynamic contexts of urban landscapes and autonomous driving scenarios, respectively. In addition, multiple studies are integrating the Level of Detail (LOD) rendering technique with 3D Gaussian Splatting to balance rendering quality and speed. Traditional mesh-based LOD strategies [Cignoni et al. 2004; Ponchio and Dellepiane 2016] create varying levels of detail in object meshes, selecting the appropriate level based on the viewer's distance to the target or the desired quality. Point-based LOD methods, like Potree [Schütz et al. 2016] and Fast-LOD [Schütz et al. 2020], are designed to efficiently render large

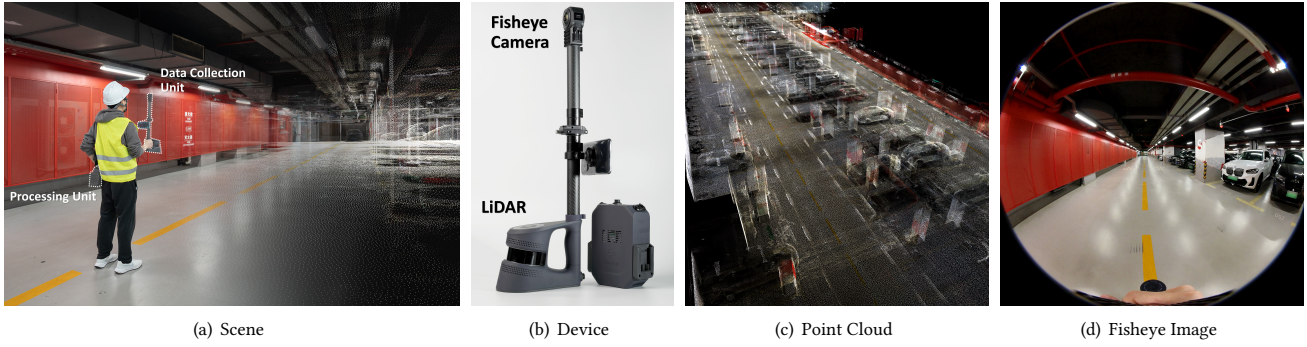


Fig. 2. Our compact Polar scanner (b) is engineered for capturing expansive garage environments (a). It is optimized for handheld operation or vehicular mounting, enabling versatile data capture in extensive spaces. At the core of Polar’s data acquisition unit lies a high-fidelity LiDAR sensor, capturing precise 3D point clouds (c), complemented by a fisheye camera that procures wide-angle 2D RGB images (d) for a complete scene modeling.

Table 1. Detailed illustrations of our GarageWorld dataset, including various datasets categorized by their environment type, geometric features, area size, number of images, point count, face count, and lighting conditions

Dataset	Category	Geometry	Aera(m^2)	Image Num	Point Num	Face Num	Lighting Condition
Campus 1	Underground	Flat & Sloped Paths	38447.86	8479	1.9B	121.9M	Uniform Lighting
Campus 2	Underground	Flat & Sloped Paths	28046.37	7772	1.4B	95.8M	Uniform Lighting
Shopping Mall 1	Indoor (Multi-floors)	Spiral & Circular Paths	32646.68	5792	1.14B	40.8M	Uneven Lighting
Shopping Mall 2	Outdoor	Spiral & Sloped Paths	13495.92	2280	0.6B	77.1M	Natural Lighting
Shopping Mall 3	Underground	Flat & Sloped Paths	30246.07	13296	1.6B	106.1M	Uniform Lighting
Office Building	Underground	With Mechanical Parking System	22159.25	9308	1.15B	72.3M	Motion Sensor Lighting
Arts Center	Underground	Flat & Sloped Paths	10392.32	5779	0.52B	31.4M	Uniform Lighting
Subway Garage	Underground	Flat & Sloped Paths	7109.12	3607	0.70B	43.5M	Uniform Lighting

3D point clouds, which is particularly beneficial for LiDAR data visualization.

Recently, Octree-GS [Ren et al. 2024] proposes representing Gaussians within an octree structure to render fine details at different viewing scales. CityGaussian [Liu et al. 2024] employs an LOD strategy for efficiently training and rendering of large-scale 3DGS. However, these methods lack on-demand rendering schemes and require high-computational devices to load complete scenes for real-time rendering, making them unsuitable for lightweight devices such as tablets or laptops. Hierarchical 3DGS [Kerbl et al. 2024] delivers promising results in rendering large-scale walk-through datasets without requiring high-performance computational devices. Nonetheless, it lacks a web-based viewer that supports rendering on lightweight devices, such as laptops and iPads. In contrast, our LetsGo method employs a multi-resolution Gaussian representation coupled with an on-demand rendering scheme. This approach achieves rendering speeds four times faster than the original 3DGS and ensures compatibility with lightweight devices, facilitating real-time rendering in large-scale garage scenes.

3 GARAGE DATA CAPTURE

3.1 Raw Data Acquisition

Scanning and modeling a large garage is a non-trivial task. Underground and indoor garages often face challenges in receiving GPS signals due to the physical barriers presented by the structures and materials surrounding them, making camera pose estimation for scanning and modeling difficult. Furthermore, there are always

large-scale texture-less regions inside a garage, *e.g.*, floors and walls. The parked vehicles often contain transparent glasses, and their surfaces are sometimes reflective. This complicates feature matching between images for camera pose estimation and 3D geometry reconstruction. Using a LiDAR sensor for scanning and modeling can provide detailed geometric information. However, the RGB color for each scanned point is not associated.

Capturing Device. To address these problems, we design a lightweight handheld scanning device named “Polar” to jointly collect color and geometric information of the garage. The data collection unit of the Polar device comprises a color fisheye camera, a LiDAR sensor, and an IMU sensor, as visualized in Fig. 2. The fisheye camera captures RGB color information in 30 FPS. It has a resolution of 6K and a field of view (FOV) of 180×180 degrees, allowing for quick and comprehensive recording of color data. The LiDAR sensor collects 3D point clouds, recording geometric information at a rate of 2.6 million points per second. With a measurement accuracy of 1 to 1.5 cm and a maximum detection distance of 50 m, it is ideal for 3D scanning of large garage scenes. The IMU sensor provides acceleration information on the device’s motion, enabling more accurate pose estimation. In addition to the data acquisition unit, we also equip the Polar device with a data processing unit consisting of a mini PC for real-time SLAM calculations. The data processing unit is powered by two removable batteries that provide more than 30 minutes of single scan endurance. With this unit, one can use a smartphone to connect with the Polar device and preview 3D point cloud reconstruction results in real-time. More information

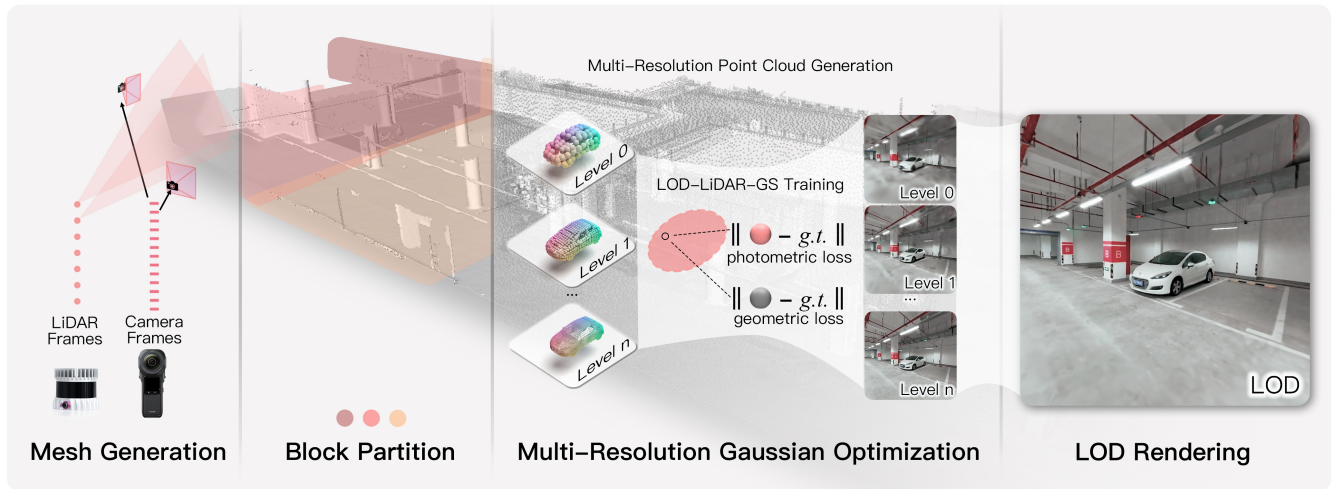


Fig. 3. Overview of our LiDAR-assisted Gaussian splatting framework. Initially, we generate a base mesh using color and depth data collected by our self-designed Polar device. The data is then partitioned into blocks for parallel and rapid processing. Next, we downsample the high-quality scanned point clouds into multi-resolution point cloud for our LOD-LiDAR-RGS (Sec. 4.2) method initialization. In addition to photometric supervision, we apply our novel unbiased Gaussian depth regularizer (Sec. 4.1) for geometric supervision. Finally, our system produces photorealistic LOD rendering results based on the optimized multi-resolution Gaussian representation.

about Polar device along with the calibration process is provided in Appendix. A.

Scanning Scheme. We use the Polar device to scan various garages for modeling and free-viewpoint rendering. The scanning trajectory for each garage is meticulously designed to emulate drive-through and parking. We collect data along each trajectory four times: one for forward-facing, one for backward-facing, one for side-left, and one for side-right, ensuring comprehensive capturing of the garage. We set the camera to auto exposure and auto ISO to accommodate complex lighting changes in the garage. For garages that are partially open-air and partially covered, the data is collected when the sunlight is weak, *i.e.*, during the early morning or evening. This ensures the images captured in the transition between open-air and covered areas share similar illumination. We also apply a short pause for data capturing at the transition area, allowing the sensor to adapt to different lighting conditions and thus ensuring the images are neither overexposed nor underexposed. For garages with motion-activated lights, we ensure the data is collected after the light turns on, maintaining consistent lighting conditions across all images. The travel speed for data collection is at around 1.0 ± 0.2 m/s, with a turning speed of 15 ± 3 %/s. To avoid motion blur in areas with insufficient light, these parameters are reduced to 0.5 m/s and 10 %/s, respectively. Some garages are very large, for example, over 30,000 square meters. Thus, we divide large garages into small subsections and collect data for each subsection. The data is fused later after collection.

3.2 GarageWorld Dataset

We collect data for eight garages¹, including six underground garages with various types of inside geometries, one indoor garage with multi-floors at Shopping Mall One, and one outdoor surface parking

¹All garage data is captured with the necessary permits.

at Shopping Mall Two. These garages comprise various challenging structures, such as sloped surfaces with distorted lines, internal circular or spiral paths, vehicle elevators, *etc.*, as shown in Fig. 4. Tab. 1 provides an overall description of the garages.

Underground Garages. Most of our captured garages are located underground. This architectural choice is prevalent in regions where above-ground space is scarce, allowing the conservation of surface area for alternative applications. Our underground garages on campus feature a single parking level, characterized by flat and sloped surfaces, and are lit by regular fluorescent light tubes affixed to the ceilings. In contrast, the garages at Shopping Mall Three and the Arts Center have vibrant design elements and superior lighting conditions. Additionally, we conduct a scan of a compact indoor garage within an office building, equipped with a mechanical parking system and featuring colored surfaces.

Indoor Garage with Multi-floor. Staking garages to multi-floor is a common design in dense urban environments. We collect data for this type of parking garage in Shopping Mall One. The different floors of this garage are connected by spiral and circular paths, which have a semi-open structure and are partially illuminated by sunlight and partially by indoor lights. Given that the lights in the shopping mall are not turned on in the early morning, we collect data for this garage during the early evening to maintain consistent illumination between different images.

Outdoor Parking. The outdoor surface parking facility is often in areas with large spaces or on the top of a commercial building. We collect data for a garage with this type located on the top of Shopping Mall Two. The entrance to this parking space is from indoor to outdoor, containing spiral and sloped paths. During daylight time, the outdoor illumination is stronger than indoor. At night, the limited dim streetlights are insufficient for photography requirements. Therefore, we conduct our data capture during the early morning

and evening when the sunlight is soft, and the illumination between indoors and outdoors is similar.

3.3 Initial Mesh Reconstruction

We employ the off-the-shell LiDAR-Inertial-Visual (LIV) SLAM [Shan et al. 2021] to estimate the relative poses of the sensor between different time steps. The LIV-SLAM system integrates a tightly coupled LiDAR-Inertial Odometry and Visual-Inertial Odometry, along with a joint optimization approach between LiDAR and camera data, for relative pose estimation. The pose estimation system leverages the unique capabilities of each sensor of our Polar device to enhance overall accuracy and robustness. The IMU delivers reliable short-term motion estimates, while the LiDAR contributes precise distance measurements. Visual sensors complement these by enriching pose estimation in environments abundant with visual features, ensuring a robust and precise outcome.

After merging the point cloud data collected at different time steps using the estimated relative pose, we apply Poisson Reconstruction [Kazhdan et al. 2006] to convert the point cloud data into a mesh. To ensure the accuracy and integrity of the resulting mesh, we also compare the reconstructed mesh to the original point cloud data to remove incorrect faces (More details in Appendix. B). This geometry-based mesh reconstruction method performs well for Lambertian surface reconstruction. However, it faces challenges for reflective and transparent surfaces, *e.g.*, vehicle glass windows, which is especially common in garage environments.

4 LIDAR-ASSISTED LOD GAUSSIAN

3D Gaussian representation excels at modeling transparent and reflective surfaces compared to a mesh representation. However, it requires a sparse 3D point cloud of the scene and accurate camera parameters obtained from SfM. As discussed previously, the large-scale garage scenes are challenging for SfM algorithms, with low lighting conditions, large texture-less regions, repetitive patterns, *etc.*, making sufficient feature correspondences between different images hard to establish. As a result, the capacity of the original 3DGS for high-quality modeling and rendering is limited.

Our Polar scanner, equipped with calibrated IMU, LiDAR, and fisheye camera sensors, effectively addresses this challenge. By integrating the unique strengths of these diverse sensors, our system achieves precise camera localization and detailed 3D point cloud generation. In the following sections, we first delve into the technical details of our novel LiDAR-assisted Gaussian splatting technique (Sec. 4.1), which incorporates a custom depth regularizer. By leveraging geometry priors derived from our RGBD scans, this method enhances the realism of rendered images and minimizes the occurrence of floater artifacts. Subsequently, we introduce an innovative framework incorporating Level-of-Detail (LOD) technology into our Gaussian training and rendering process (Sec. 4.2). This framework utilizes a multi-resolution point cloud as its input, significantly boosting rendering speeds. Moreover, we show how it can facilitate rendering expansive garage environments on lightweight devices through a specialized web-based renderer (Sec. 4.3). Fig. 3 provides an overview of our LiDAR-assisted Gaussian splatting framework.

4.1 Gaussian Splatting with LiDAR Inputs

3DGS [Kerbl et al. 2023] represents 3D points with 3D Gaussians, parameterized by position μ , opacity α , anisotropic covariance Σ , and spherical harmonic (SH) coefficients representing view-dependent color c . The projection from 3D Gaussians to 2D images [Zwicker et al. 2001b] is given by

$$\Sigma' = JW\Sigma W^T J^T, \quad (1)$$

where J represents the Jacobian of the affine approximation of the projective transformation, and W corresponds to the viewing transformation.

The goal is to optimize the Gaussian parameters so that the rendered images from the 3D Gaussians are as close to their ground truth (GT) images as possible.

A standard three-dimensional Gaussian sphere can be transformed into an ellipsoid of arbitrary shape within space by applying a covariance matrix Σ . Additionally, so as to ensure the semi-definiteness of the covariance matrix during the optimization process, Kerbl *et al.* proposes to optimize a scaling matrix S and rotation matrix R , and compute the covariance matrix as:

$$\Sigma = RSS^T R^T, \quad (2)$$

where S is parameterized as a 3D vector and R is parameterized as quaternion, a 4D vector with unit norm.

Since conventional SfM approaches fail in large garage environments due to hard correspondence establishment between texture-less and transparent regions, we use our Polar device with a LiDAR sensor to scan point clouds of the garages. Considering the originally scanned point clouds contain noise, we resample a set of new points from the reconstructed mesh with a uniform sampling strategy. These resampled points, in conjunction with the camera parameters, are used to train the 3DGS representations.

In addition to the image reconstruction loss in the original Gaussian splatting, we further introduce a depth-regularizer for our LiDAR-assisted 3DGS training, which incorporates depth priors derived from the high-quality LiDAR data during training. We denote this method as LiDAR-GS and the original 3DGS method with LiDAR-assisted point cloud for Gaussian initialization as 3DGS*.

Depth Regularizer. Inspired by the depth calculation from NeRF [Mildenhall et al. 2021], we utilize the rasterization pipeline of Gaussians to compute the depth of each Gaussian primitive:

$$D_G = \sum_{i \in N} d_i \alpha_i T_i, \quad T_i = \prod_{j=1}^{i-1} (1 - \alpha_j), \quad (3)$$

where D_G is the rendered depth and d_i is the depth of each Gaussian splat in camera perspective.

It should be noted that the center of the Gaussian is not directly employed for depth computation. Due to variations in the shape and orientation of the Gaussian, the depth at the precise point where the ray intersects the Gaussian deviates from the depth at its center. Our approach computes the expected depth at the specific point of intersection with the Gaussian as follows:

$$d_i = \frac{1}{l} \left(p_2 - \frac{(\Sigma^{-1})_{0,2}}{(\Sigma^{-1})_{2,2}} (x_0 - p_0) - \frac{(\Sigma^{-1})_{1,2}}{(\Sigma^{-1})_{2,2}} (x_1 - p_1) \right) \quad (4)$$

where $\mathbf{p} = [p_0, p_1, p_2]$ represents the position of the Gaussian center in the ray space, and Σ is the 3×3 covariance matrix. $(\cdot)_{m,n}$ represents the corresponding element in the matrix. For detailed derivation and understanding of this process, please refer to Appendix C.

Given the K captured views, we compute the depth loss using the following equation:

$$\mathcal{L}_{\text{depth}} = \sum_{k \in K} \left\| D_G^k - D^k \right\|_1, \quad (5)$$

where D^k represents the k^{th} inherent depth prior from LiDAR data.

The total loss function is as follows:

$$\mathcal{L}_{\text{total}} = \mathcal{L}_{\text{rgb}} + \lambda_{\text{depth}} \mathcal{L}_{\text{depth}}, \quad (6)$$

where \mathcal{L}_{rgb} is the RGB image reconstruction loss, following the original 3DGS, and λ_{depth} is the weight for our depth term. By incorporating the depth constraint, our LiDAR-GS effectively minimizes the occurrence of floating artifacts and aligns the Gaussian kernel more closely with the depth information inherent in the LiDAR data.

4.2 Multi-Resolution Representation

The original 3D Gaussian representation requires a vast number of 3D Gaussians, making it resource-intensive and inefficient for lightweight devices. However, simultaneously loading all Gaussians of the entire scene is inefficient and unnecessary for rendering a specific view.

Inspired by advanced rendering techniques [Schütz et al. 2016] for massive LiDAR point clouds, we introduce a multi-resolution Gaussian framework called LOD-LiDAR-GS. This framework integrates the Level-of-Detail (LOD) rendering to the LiDAR-GS, making it suitable for various devices. We represent the 3D scene with Gaussians at different resolution levels. When initializing the multi-resolution Gaussians, each Gaussian is assigned an LOD attribute, alongside its original attributes like 3D position, spherical harmonic coefficients, and opacity, to support our LOD rendering. The LOD value dynamically adjusts the cloning and splitting threshold during training. This multi-resolution representation enables fast and lightweight rendering on web-based devices.

Multi-Resolution Gaussian Initialization. We first construct multi-resolution point cloud data for Gaussian initialization. Our Polar device generates dense point clouds with superior accuracy and consistency, even in challenging garage conditions. We use a spacing attribute, τ , to represent the resolution of a point cloud, defined as the minimal distance between points. The finest resolution corresponds to the original point cloud sampled from our reconstructed mesh at the lowest τ . We then increase τ to 2τ and downsample the point cloud to derive a coarser point cloud, repeating until the point count drops below a threshold, ϵ_p . Points in the finest level get an LOD value of $N = L - 1$, and those in the coarsest level get an LOD value of $N = 0$. We set τ to 4.0 cm and ϵ_p to 10,000 points.

ALGORITHM 1: Octree Construction for LOD-LiDAR-GS

Input : A set of multi-resolution Gaussians stored in .ply files
Output : Gaussian in Octree structure stored in .bin files

```

// Initialization
Create an octree with depth L
Compute bounding box B that covers all Gaussian levels
Initialize queue = {root of octree, B, lvl = 0}
// First loop: Distribute Gaussians into octree nodes
while length(queue) > 0 do
    currentNode ← queue.pop()
    foreach childNode of currentNode do
        Assign bounding box B_child and
        lvl = {currentNode.lvl} + 1 to childNode
        queue.push({childNode, B_child, lvl})
    end
    Read Gaussians from level_{currentNode.lvl}.ply
    Distribute Gaussians within currentNode.B
end
Initialize queue = {root of octree, B, lvl = 0}
byteOffset, byteSize = 0, 0
// Second loop: Prune empty nodes and store data
while length(queue) > 0 do
    currentNode ← queue.pop()
    foreach childNode of currentNode do
        if childNode.numPoints > 0 then
            queue.push({childNode, childNode.B, lvl})
        end
    end
    byteSize = size(currentNode.points)
    Flush currentNode.points into octree.bin file
    Flush currentNode.B, currentNode.numPoints,
    byteOffset, byteSize into hierarchy.bin file
    byteOffset ← byteOffset + byteSize
end

```

The downsampling operation employs an approximate Poisson-disk sampling method from the PotreeConverter library [Schütz et al. 2016].

LOD-LiDAR-GS Training. In contrast to LiDAR-GS, our LOD-LiDAR-GS framework processes a multi-resolution point cloud, wherein each resolution level has a distinct LOD value. We devise a new training strategy to handle the complexity caused by multi-resolution input effectively. We initialize a Gaussian model for each resolution level, which operates independently during optimization. Following the original 3DGS [Kerbl et al. 2023], the decision to clone or split a Gaussian is based on threshold values for position gradients σ_{pos} and variance σ_{var} . We introduce a scaling factor s , which varies with the LOD value l of each level, modifying the thresholds as $s \cdot \sigma_{pos}$ and $s \cdot \sigma_{var}$:

$$s_k = \min(\beta_s^{L-1-l}, s_{max}), \quad l \in [0, L-1] \quad (7)$$

where β_s and s_{max} are hyperparameters set to $\sqrt{2}$ and 4.0 respectively.

In our approach, the Gaussian representation at the lower resolution levels is employed to encapsulate the low-frequency content

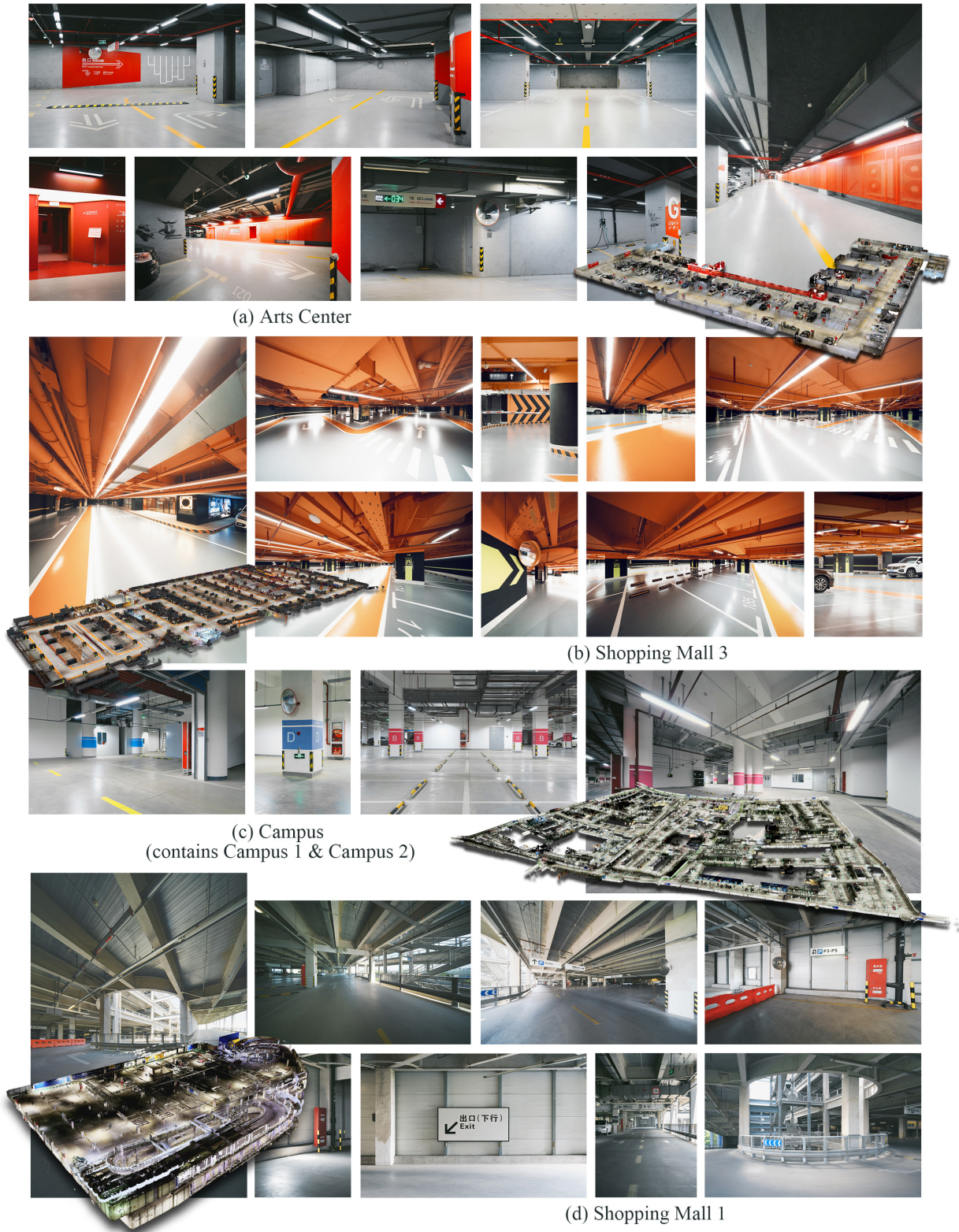


Fig. 4. Visualization of examples from our GarageWorld dataset.

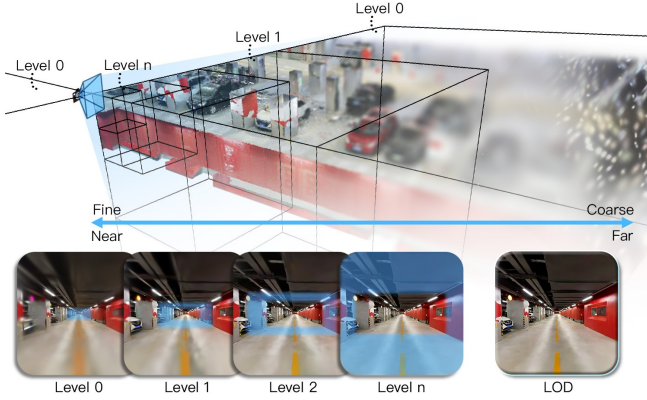


Fig. 5. Illustration of our LOD-LiDAR-GS within an Octree Structure, accompanied by an LOD rendering strategy. Distance varies from near to far, with Gaussian level resolution transitioning from fine to coarse. The bottom row illustrates the level composition in the rendered view.

of the scene, while higher resolution levels utilize finer Gaussians to capture the intricate high-frequency details. To use our multi-resolution Gaussian models for image rendering, we adopt a technique analogous to LOD rendering used in traditional computer graphics pipelines. Gaussian subsets from each resolution level are selected based on the rendering camera’s viewing frustum and the projected depth d of each Gaussian. The appropriate Gaussian level $L^{(d)}$ is determined as:

$$L^{(d)} = \text{clamp}(\lfloor L^{1-d/d_{max}} \rfloor, 0, L - 1) \quad (8)$$

where d_{max} is the maximum depth value projected onto the training viewpoint from the point cloud.

During training, we select portions of Gaussians from different resolution levels based on depth ranges to accurately predict the image. We compute the loss by comparing model predictions with ground truth images. Our random-resolution-level (RRL) training strategy renders each training sample with a 50% probability using either the LOD strategy from multiple levels or a single Gaussian level, preventing overfitting and biases in camera pose distribution.

4.3 Web-based Lightweight Renderer

With the proposed multi-resolution Gaussian representation, our LOD-LiDAR-GS significantly enhances rendering efficiency. Instead of using a large number of 3D Gaussians for each image, LOD-LiDAR-GS dynamically selects Gaussian subsets from different resolution levels based on depth ranges. This reduces the complexity of sorting, projection, and accumulation operations, thereby accelerating rendering speed. On GPU systems such as the NVIDIA RTX 3090, we implement a 3D Gaussian viewer based on the original 3DGS SIBR viewer. By integrating our LOD rendering strategy, as detailed in Equation 8, we achieve approximately a 4x increase in rendering speed. Additionally, we introduce a web-based, on-demand renderer developed with JavaScript and WebGL, which supports real-time rendering on lightweight devices. Unlike mainstream lightweight Gaussian renderers [Face 2024; Kwok 2023], which load all Gaussians into VRAM simultaneously, our renderer dynamically loads

only the necessary data into memory according to the current viewpoint and LOD strategy. This method avoids the need for full data loading, enabling the rendering of large-scale environments on web platforms.

Converting Multi-Resolution Gaussians into Octree Structure. Our multi-resolution Gaussian representation is well-suited for storage within an Octree structure, with Gaussians at each level efficiently stored in the nodes at the corresponding depth of the Octree. We begin by constructing an Octree of depth L , where the root node host level 0 and the leaf nodes contain the finest level, $L - 1$. Intermediate levels are stored at the inner nodes of the Octree. We outline the conversion of our Gaussian representation into the Octree format in Algorithm 1.

Coarse-to-Fine Rendering. Rendering large-scale garage scenes requires managing a substantial number of Gaussians, often exceeding in-memory storage capacity. To address this, we implement a coarse-to-fine loading and rendering scheme that facilitates real-time rendering on resource-constrained devices. Initially, low-resolution Gaussian levels are preloaded into memory at viewer initialization. These levels occupy minimal storage and are accessed frequently during subsequent rendering cycles. As shown in Fig. 5, to render high-frequency details, our system dynamically selects high-resolution octree chunks from disk based on the viewer’s frustum and the conditions set by our LOD rendering strategy, as outlined in Equation 8. The rendering process begins with a traversal of the entire octree, determining each node’s visibility based on the center position of the node’s bounding box. A second traversal then loads visible Gaussian data into a buffer, continuing until either the traversal is complete or the number of loaded Gaussians reaches the maximum capacity. The buffer is updated by replacing preloaded Gaussians with newly loaded high-resolution Gaussians, which are then dispatched to a WebGL worker for rendering. Recent works, such as OCT-GS [Ren et al. 2024] and LoG [Shuai et al. 2024], can also be structured into an octree format. However, OCT-GS fails to represent the entire scene at certain levels, making it unsuitable for our lightweight rendering strategy. Additionally, LoG does not provide a solution for lightweight rendering.

5 EXPERIMENTAL RESULTS

5.1 Training Details

All experiments are conducted on an NVIDIA RTX A6000 GPU using the PyTorch Framework. Given the large scale of our scenes and the initialization with LiDAR point clouds, we set the scaling learning rate to 0.0015 and the initial position learning rate for Gaussian primitives to 0.000016. We disable the opacity reset option and delay the start of the Gaussian densification step to 75,000 iterations. The total number of iterations is empirically set to twenty times the number of captured images. We use a spherical harmonics (SH) degree of 2 and set λ_{depth} to 0.8. We employ a partitioning strategy similar to [Tancik et al. 2022], expanding each block outward by 30% to address the poor reconstruction quality on the boundaries. The overall end-to-end duration, including data capture, preprocessing, and training, typically ranges from 12 to 16 hours. Each scene is divided into 3 to 10 blocks, depending on its complexity. The training

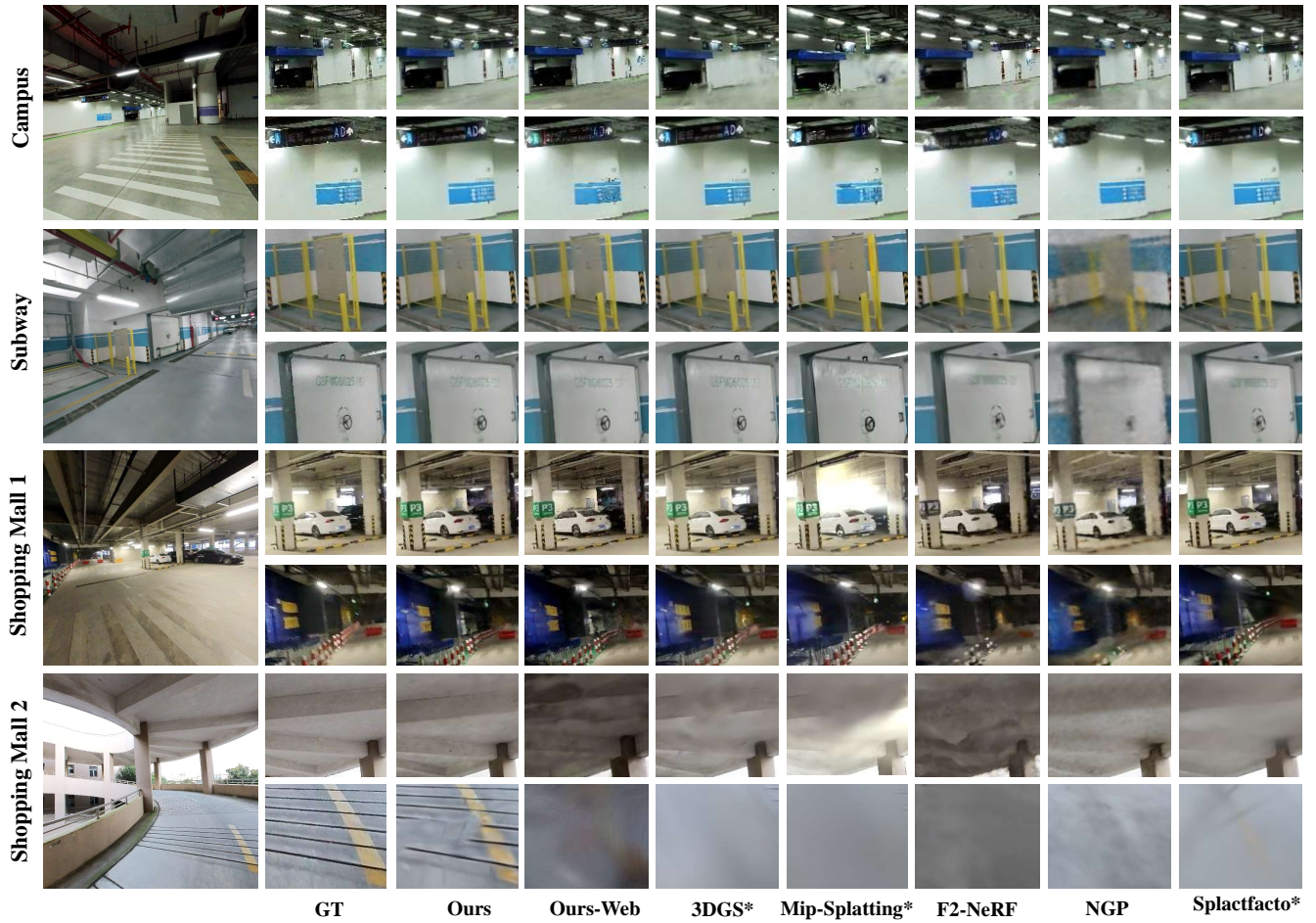


Fig. 6. Qualitative comparison between our LOD-LiDAR-GS, 3DGS*, Mip-Splatting*, F2-NeRF, NGP and Splatfacto* on the various datasets. Here, we use a superscript * to denote their Gaussian primitives are initialized according to our LiDAR-assisted 3D point cloud.

Table 2. Quantitative comparison among our LOD-LiDAR-GS, 3DGS*, Mip-Splatting*, F2-NeRF, NGP, Splatfacto*, OCT-GS*, and LoG-GS* on the various datasets.

Method	GarageWorld			ScanNet++			KITTI-360		
	PSNR↑	SSIM↑	LPIPS↓	PSNR↑	SSIM↑	LPIPS↓	PSNR↑	SSIM↑	LPIPS↓
3DGS*	23.52	0.822	0.412	27.41	0.902	0.149	20.39	0.698	0.289
Mip-Splatting*	22.08	0.791	0.448	25.74	0.898	0.179	20.19	0.682	0.318
F2-NeRF	18.88	0.739	0.552	23.59	0.888	0.237	18.60	0.653	0.414
NGP	20.68	0.734	0.507	28.72	0.896	0.230	21.21	0.655	0.406
Splatfacto*	25.45	0.793	0.261	28.35	0.906	0.065	14.76	0.481	0.381
OCT-GS*	25.19	0.782	0.315	31.55	0.941	0.063	21.52	0.692	0.322
LoG-GS*	21.53	0.737	0.278	27.80	0.907	0.086	18.62	0.671	0.300
Ours (LOD-LiDAR-GS)	25.77	0.812	0.210	29.19	0.927	0.064	24.53	0.811	0.167
Ours (Web)	22.56	0.730	0.211	22.79	0.824	0.140	19.20	0.586	0.247

duration for each block varies from 1.5 to 4 hours, based on the size of the point cloud and the number of images. In a few cases, irregular shapes in underground garages result in particularly large blocks, extending the training time to over 8 hours.

Training Image Selection and Pre-processing. Regarding training view selection for each block, camera views originating within the partition bounds are retained. Furthermore, for camera views positioned outside the partition, we project the mesh in the partition block and the original mesh onto each camera view and compute the projected pixel overlap ratio between the quadrilateral-partitioned

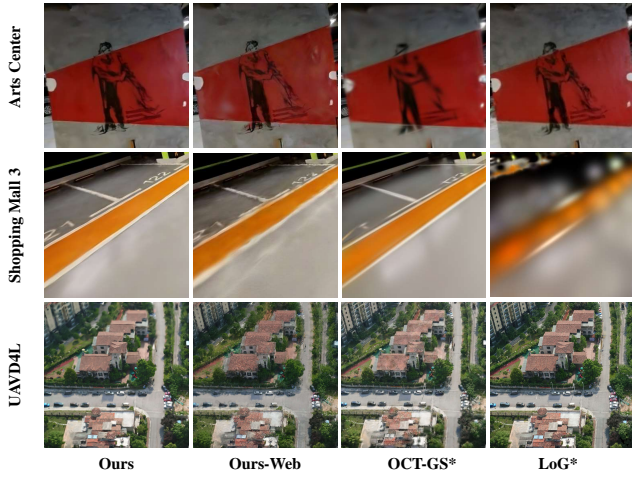


Fig. 7. Qualitative comparison of our method and concurrent works, including recent OCT-GS* and LoG* methods, on the GarageWorld and UAVD4L datasets.

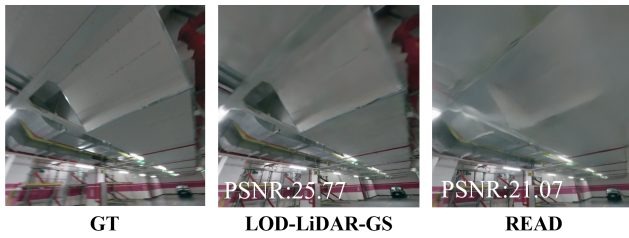


Fig. 8. Qualitative and Quantitative comparison of our method and READ approach on the GarageWorld datasets.

mesh and the whole mesh. Views with a ratio exceeding a threshold of 0.8 are retained. The original Gaussian framework does not support direct input of fisheye images. To retain more information from the images, we avoided traditional fisheye distortion correction. Instead, we split a single fisheye image into five pinhole images. Specifically, the fisheye image is projected onto a hemispherical surface. Then, five virtual cameras, each oriented at 45 degrees to the top, bottom, left, right, and straight ahead, reproject the hemispherical image into their respective views. This process generates new images and extrinsic parameters. Additionally, since the downward-facing view includes part of the capturing device, we use a mask to obscure this portion of the image.

5.2 Comparison

Datasets. We compare our approach with state-of-the-art methods and concurrent works on various challenging datasets, including our **GarageWorld**, **KITTI-360** [Liao et al. 2022] (large outdoor street scene), and **ScanNet++** [Yeshwanth et al. 2023] (indoor scene characterized by complex geometry and variable lighting). For each dataset, we use 10% of the images as test sets and the remaining 90% as training sets.

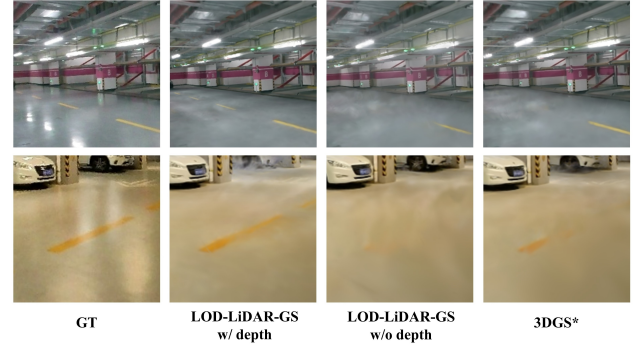


Fig. 9. Qualitative ablation study on depth regularization within our large-scale GarageWorld dataset clearly demonstrates improvements in resolving the floater problem on the ground.

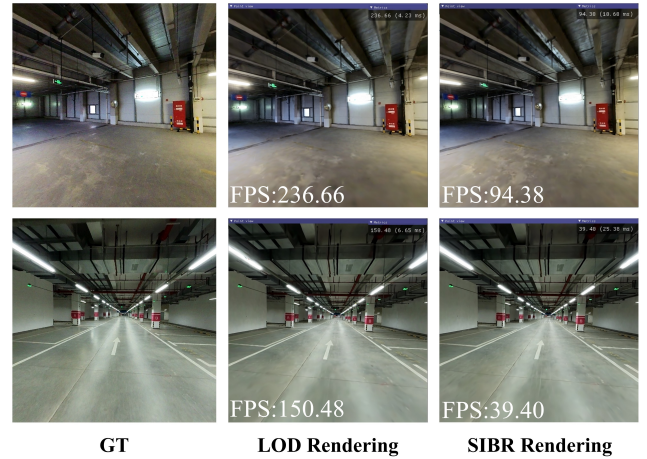


Fig. 10. Ablation study on our LOD rendering strategy demonstrates that our real-time LOD renderer operates approximately 3-4 times faster than the original 3DGS SIBR viewer when tested on an NVIDIA RTX 3090 GPU.

Competing Methods. We compare our method against a suite of 3DGS approaches, including **3DGS*** [Kerbl et al. 2023], **Mip-Splatting*** [Yu et al. 2024], and **Splactfacto*** [Tancik et al. 2023], as well as recent concurrent work, including **OCT-GS*** [Ren et al. 2024] and **LoG*** [Shuai et al. 2024]. Additionally, we benchmark our approach against recent implicit representation methods, namely **F2-NeRF** [Wang et al. 2023] and **Instant-NGP** [Müller et al. 2022]. To extend recent 3DGS-based methods to large-scale garage scenes, we initialize them with our LiDAR-derived point clouds instead of SFM point clouds, enabling their application to challenging garage environments. Methods utilizing our LiDAR-derived point clouds are denoted with an asterisk (*).

Quantitative Comparison Results. For quantitative comparisons, we use Peak Signal-to-Noise Ratio (PSNR), Structural Similarity (SSIM), and Learned Perceptual Image Patch Similarity (LPIPS) [Zhang et al. 2018] as metrics to evaluate rendering quality. The results of these comparisons are presented in Tab. 2. Our LOD-LiDAR-GS

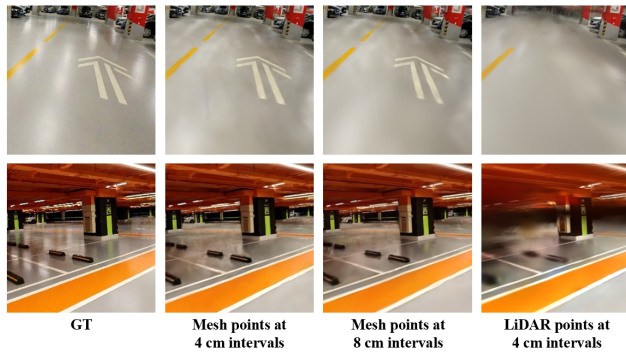


Fig. 11. Qualitative ablation study on different input point cloud qualities demonstrates that using point clouds sampled from the mesh significantly enhances rendering quality.

method consistently achieves the best results on large-scale scene datasets, such as our GarageWorld dataset and the KITTI-360 dataset. On the small-scale scene dataset ScanNet++, our LOD-LiDAR-GS approach achieves the second-best results. From the last two rows of Tab. 2, our web renderer demonstrate comparable performance on lightweight devices (MacBook Air with M2 clip).

Qualitative Comparison Results. As shown in Fig. 6, both 3DGS* and Splactfacto* tend to generate floating Gaussian points around scene surfaces, resulting in blurriness and poor rendering quality. F2-NeRF performs well on the relatively small-scale ScanNet++ dataset but suffers from artifacts in the large-scale KITTI-360 dataset and blurriness in our GarageWorld dataset. Instant-NGP, which utilizes hash encoding, produces notably blurry results in large-scale scenes. In contrast, our method demonstrates the highest rendering quality across various scenarios. We also compared our method with concurrent works such as OCT-GS* and LoG*. As shown in Fig. 7, our approach achieves the best rendering quality on both our GarageWorld and the UAVD4L datasets (recently proposed and used in LoG*). Our web-based results also show comparable visual quality. Moreover, we evaluate our method against the READ method [Li et al. 2023] which also uses LiDAR as input. Fig. 8 presents the qualitative and quantitative results, showing that our method can recover more high-frequency details.

Rendering Performance of Web-based Renderer. Additionally, we evaluate the performance of our web-based renderer on various devices. On a high-performance desktop equipped with an i9-10900X CPU and a Samsung SSD T5 Disk, it takes 1.36 seconds to load approximately 2 million 3D Gaussians. On a MacBook laptop with an Apple M2 CPU and Apple SSD AP0512Z Disk, the load time for the same number of 3D Gaussians is 1.29 seconds. Combining these newly loaded 3D Gaussians with an additional 3 million pre-loaded Gaussians, both devices maintain a rendering frame rate of 60 FPS. Due to browser memory constraints, we restrict the 3D Gaussian data loaded for rendering to a maximum of 2 GB. Furthermore, the web renderer uses CPU-based sorting, which is slower than the CUDA-based sorting employed by the original 3DGS renderer.

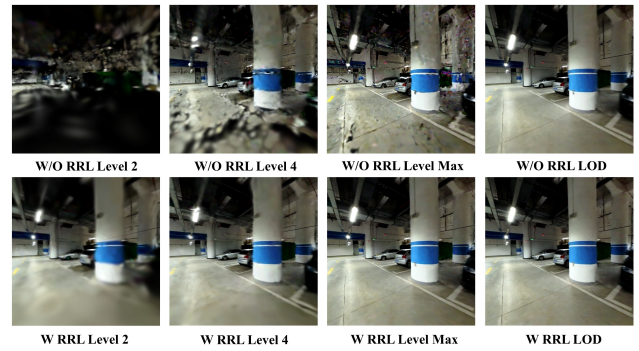


Fig. 12. Qualitative ablation study on the random-resolution-level (RRL) training strategy reveals that our RRL approach effectively addresses the overfitting issue at a certain level, influenced by the camera distribution.

To balance rendering quality and performance, we adopt our LOD rendering strategy that adjusts the number of loaded 3D Gaussians.

5.3 Ablation Study

In this section, we perform ablation studies to validate the effectiveness of each component of our approach.

Depth Regularization. Using only photometric loss constraints can easily produce artifacts, such as floaters, in large-scale scene reconstruction. To address this, we introduce an additional depth regularization term to enforce geometric constraints. As shown in Fig. 9, we evaluated the impact of our depth regularization module across various scenes. Our results demonstrate that the **LOD-LiDAR-GS** method effectively mitigates floaters on the ground when depth regularization is applied.

Input Point Cloud Qualities. Relying solely on high-density point clouds can lead to computational inefficiencies without significantly enhancing reconstruction quality. To investigate this, we conducted an ablation study assessing the impact of varying point cloud qualities on our reconstruction results. As shown in Fig. 11 and Tab. 3, we evaluated the performance of our **LOD-LiDAR-GS** method using point clouds sampled from the mesh at various intervals, alongside original LiDAR point clouds downsampled to 4 cm intervals. Our findings indicate that while higher densities yield more detailed reconstructions, the benefits plateau beyond a certain threshold. Conversely, lower densities still deliver robust performance with reduced computational costs. To balance training time and reconstruction quality, we selected 4 cm intervals for sampling from the mesh. Notably, using original LiDAR point clouds directly results in poorer outcomes compared to mesh-sampled point clouds, particularly in garage environments where objects are smaller and geometrically simpler. Thus, we opted for point clouds sampled from the mesh at 4 cm intervals, which offer superior reconstruction quality while maintaining efficiency.

LOD Rendering Strategy. Next, we ablate the LOD rendering strategy. Based on our multi-resolution representation, we select Gaussian subsets from various resolution levels according to depth ranges, following the LOD rendering strategy outlined in Equation 8. This

Table 3. Quantitative ablation study on different input point cloud qualities and corresponding training times across two datasets. Point clouds sampled from the mesh at varying intervals and original LiDAR point clouds downsampled to 4 cm intervals. The training times are based on tests performed with an NVIDIA RTX A6000 GPU.

Point Cloud Density	Arts Center					Shopping Mall 3				
	PSNR↑	SSIM↑	LPIPS↓	Number of Gaussians	Training Time	PSNR↑	SSIM↑	LPIPS↓	Number of Gaussians	Training Time
2 cm (Mesh)	25.87	0.862	0.317	17698464	10:55:07	25.01	0.836	0.320	36042237	31:01:11
6 cm (Mesh)	25.52	0.854	0.340	2300174	02:47:02	24.73	0.827	0.340	4559012	06:35:14
8 cm (Mesh)	25.29	0.848	0.348	1306965	02:15:16	24.49	0.821	0.348	2566219	04:53:08
10 cm (Mesh)	25.08	0.843	0.356	836921	02:02:50	24.21	0.814	0.357	1627634	04:06:29
4 cm (LiDAR)	23.11	0.816	0.370	10024717	03:03:03	21.52	0.764	0.399	21162613	04:39:05
4 cm (Mesh)	25.70	0.858	0.330	4997081	02:23:27	24.91	0.832	0.331	10015908	10:58:39



Fig. 13. Applications of our system: (a) Autonomous vehicle parking. Our diverse garage scenes facilitate training algorithms for generating parking trajectories under different scenarios; (b) Real-time localization & navigation in challenging garage environments; (c) VFX demonstration. Through an analysis of the animation in the reference video, we extract the poses of several keyframes, which enable our system’s renderer to generate corresponding video segments and produce realistic visual effects.

strategy significantly reduces the complexity of sorting, projection, and accumulation operations involved with 3D Gaussians, thereby accelerating the rendering speed. As shown in Fig. 10, our real-time viewer, integrated with the LOD rendering technique, is about 3-4 times faster than 3DGS’s SIBR viewer with similar rendering quality.

Random-Resolution-Level (RRL) Training Strategy. During training, directly applying the LOD rendering strategy to render images and optimize the loss can lead to overfitting at certain resolution levels in specific scene regions. We propose a random-resolution-level (RRL) training strategy to address this issue. As shown in Fig. 12, our RRL training strategy mitigates the overfitting problem and remains robust to variations in the distribution of input cameras.

6 GARAGEWORLD

We introduce the first large-scale garage dataset, **GarageWorld**, captured with our Polar device. This dataset comprises eight large garages, featuring six underground garages, one outdoor parking lot, and one multi-floor indoor garage. Fig. 4 visualizes the 3D models and rendered images of a subsection of these garages using our method. Our rendering pipeline and the GarageWorld dataset are designed to support a wide range of applications, which are further detailed in the following sections.

Data Generation and Testbed for Autonomous Driving. Our developed 3D reconstruction of large-scale garage scenes with enhanced real-time rendering can support various autonomous driving algorithms. The GarageWorld dataset provides diverse driving scenarios, including tight parking spaces and complex geometric layouts,

which are instrumental for training algorithms in autonomous parking and navigation path planning. Additionally, our LetsGo pipeline further aids vehicle parking by supplementing sensor data, particularly in low-light garage conditions. Our LiDAR-assisted Gaussian primitives allow rigorous testing in a virtual setting, prompting safe and efficient parking solutions. Fig. 13(a) illustrates how our approach generates rear-view images, allowing vehicles to accurately estimate distances and navigate tight spaces, thereby avoiding collisions and accelerating the development and deployment of safe autonomous driving technologies.

Real-time Localization and Navigation. Our LiDAR-assisted garage modeling and rendering provide accurate 3D references, significantly enhancing autonomous vehicle localization and navigation, particularly in challenging indoor or underground garages where traditional methods struggle. Fig. 13(b) presents an example of real-time localization and navigation. Additionally, our web-based rendering engine represents expansive 3D garage maps and navigation trajectories on lightweight devices with limited computational capacity, delivering smooth real-time interactions and superior rendering performance.

VFX Production. Our reconstructed garage datasets and real-time rendering capabilities significantly enhance VFX production by providing a robust foundation for creating realistic backgrounds and seamlessly integrating CGI elements into live-action footage. Inspired by the highway chase in "The Matrix Reloaded", our LetsGo pipeline excels in rendering complex garage scenes, offering precise control over elements like exposure time and motion blur. We created a VFX video production to showcase our technology using our

reconstructed garage models (Fig. 13(c)) in the supplementary video. We downloaded a video depicting highway chase scenes with dynamic viewing angles of a rapidly moving motorcycle. By extracting and aligning camera trajectories with our models and synthesizing motion blur, we created immersive visual effects that convincingly depict a chase within a garage environment. Our approach supports the exploration of diverse camera angles and compositions in real-time while ensuring visual consistency between real and virtual components, significantly reducing the need for reshoots and streamlining the production process.

7 LIMITATIONS AND DISCUSSIONS

Although our rendering results exhibit realism and we showcase various applications, our workflow still possesses certain limitations. Here we present a detailed analysis and explore further potential applications.

Firstly, our method focuses on large-scale garage scenes and relies on our lightweight 3D scanner to provide high-quality LiDAR point clouds, color images, and corresponding camera information. Although we have also validated the effectiveness of our method on other open-source datasets, it is important to explore the use of even lighter devices for scanning and rendering large-scale scenes, such as smartphones equipped with depth sensors. Additionally, we have currently collected data from eight large-scale garages, but it is necessary to gather more garage data to contribute to the community and facilitate further research on garage modeling and rendering.

As a method based on image rendering, our approach achieves highly realistic rendering effects, almost indistinguishable from real scenes. However, the existing pipeline does not support modifying lighting conditions. This requires us to carefully design the shooting process according to the lighting conditions, limiting the applicability of our method in various scenarios. Enabling rendering and editing of large-scale scenes under different lighting conditions is a meaningful direction that deserves further investigation. Our open-source dataset provides a foundation for the community to conduct research in these directions, allowing for advancements in this field. Also there are switching artifacts primarily caused by loading different Gaussian levels. These artifacts can be mitigated by interpolating between adjacent Gaussian levels during switching. [Kerbl et al. 2024] successfully achieves smooth level transitions using a linear interpolation scheme. We will explore this approach and decrease the switching artifacts in future work.

Furthermore, there are additional directions and applications worth exploring. Inspired by SMERF [Duckworth et al. 2024], one potential research direction is to investigate streaming transmission methods for Gaussian kernels, enabling the distribution and on-the-fly rendering of large-scale scene data. Additionally, there are city generation methods such as InfiniCity [Lin et al. 2023] and CityDreamer [Xie et al. 2024], which leverage Generative Adversarial Networks (GANs) [Goodfellow et al. 2014] to achieve rapid modeling of large-scale scenes. We intend to study large-scale scene generation based on 3D Gaussian representations. This fully explicit representation can be easily integrated into existing computer graphics workflows and achieve superior rendering effects.

8 CONCLUSION

For many of us, our daily lives begin with a safe departure from a garage and end with a safe arrival. The garage serves as the origin of our journey to innovation. This paper has contributed a handheld Polar device for data collection, a GarageWorld dataset, LiDAR-assisted Gaussian splatting for scene representation, and an LOD-based rendering technique that allows web-based rendering on consumer-level devices. Benefiting from these innovations, we successfully reconstruct various garages with diverse and challenging environments, allowing real-time rendering from any viewpoint on lightweight devices. Experimental results on the collected and two public datasets have demonstrated the effectiveness of our approach. Our GarageWorld, along with the reconstructed 3D model and real-time rendering, enables a set of applications, including training data generation and testbed for autonomous driving algorithms, real-time assistance for autonomous vehicle localization, navigation, and parking, as well as VFX production. Our current contributions mainly focus on the perception of the world, and enables downstream recognition tasks. In the future, we will also explore garage generation, continuing to push the boundary of garage modeling and accomplishing a closure from perception, recognition, and generation.

ACKNOWLEDGMENTS

The authors would like to thank Shanghai Municipal Big Data Center for coordinating the collection of garage data. This work was supported by National Key R&D Program of China (2022YFF0902301), NSFC programs (61976138, 61977047), STCSM (2015F0203-000-06), and SHMEC (2019-01-07-00-01-E00003). We also acknowledge support from Shanghai Frontiers Science Center of Human-centered Artificial Intelligence (ShangHAI) and MoE Key Lab of Intelligent Perception and Human-Machine Collaboration (ShanghaiTech University).

REFERENCES

- Sameer Agarwal, Yasutaka Furukawa, Noah Snavely, Ian Simon, Brian Curless, Steven M Seitz, and Richard Szeliski. 2011. Building Rome in a day. *Commun. ACM* 54, 10 (2011), 105–112.
- Kara-Ali Aliev, Artem Sevastopolsky, Maria Kolos, Dmitry Ulyanov, and Victor Lempitsky. 2020. Neural point-based graphics. In *Computer Vision—ECCV 2020: 16th European Conference, Glasgow, UK, August 23–28, 2020, Proceedings, Part XXII* 16. Springer, 696–712.
- Jonathan T Barron, Ben Mildenhall, Matthew Tancik, Peter Hedman, Ricardo Martin-Brualla, and Pratul P Srinivasan. 2021. Mip-nerf: A multiscale representation for anti-aliasing neural radiance fields. In *Proceedings of the IEEE/CVF International Conference on Computer Vision*. 5855–5864.
- Jonathan T Barron, Ben Mildenhall, Dor Verbin, Pratul P Srinivasan, and Peter Hedman. 2022. Mip-nerf 360: Unbounded anti-aliased neural radiance fields. In *Proceedings of the IEEE/CVF Conference on Computer Vision and Pattern Recognition*. 5470–5479.
- Hriday Bavle, Jose Luis Sanchez-Lopez, Claudio Cimorelli, Ali Tourani, and Holger Voos. 2023. From SLAM to situational awareness: Challenges and survey. *Sensors* 23, 10 (2023), 4849.
- Mihai Bujanca, Xuesong Shi, Matthew Spear, Pengpeng Zhao, Barry Lennox, and Mikel Luján. 2021. Robust SLAM systems: Are we there yet?. In *2021 IEEE/RSJ International Conference on Intelligent Robots and Systems (IROS)*. IEEE, 750–757.
- Simone Ceriani, Carlos Sánchez, Pierluigi Taddei, Erik Wolfart, and Vitor Sequeira. 2015. Pose interpolation SLAM for large maps using moving 3d sensors. In *2015 IEEE/RSJ international conference on intelligent robots and systems (IROS)*. IEEE, 750–757.
- David Charatan, Sizhe Lester Li, Andrea Tagliasacchi, and Vincent Sitzmann. 2024. PixelSplat: 3d Gaussian splats from image pairs for scalable generalizable 3d reconstruction. In *Proceedings of the IEEE/CVF Conference on Computer Vision and Pattern Recognition*. 19457–19467.

- Anpei Chen, Zexiang Xu, Andreas Geiger, Jingyi Yu, and Hao Su. 2022. TensorRF: Tensorial Radiance Fields. In *European Conference on Computer Vision (ECCV)*.
- Anpei Chen, Zexiang Xu, Fuqiang Zhao, Xiaoshuai Zhang, Fanbo Xiang, Jingyi Yu, and Hao Su. 2021. Mvsnr: Fast generalizable radiance field reconstruction from multi-view stereo. In *Proceedings of the IEEE/CVF International Conference on Computer Vision*. 14124–14133.
- Kai Cheng, Xiaoxiao Long, Kaizhi Yang, Yao Yao, Wei Yin, Yuexin Ma, Wenping Wang, and Xuejin Chen. 2024. Gaussianpro: 3d Gaussian Splatting with progressive propagation. In *Forty-first International Conference on Machine Learning*.
- Paolo Cignoni, Fabio Ganovelli, Enrico Gobbetti, Fabio Marton, Federico Ponchio, and Roberto Scopigno. 2004. Adaptive tetrapuzzles: efficient out-of-core construction and visualization of gigantic multiresolution polygonal models. *ACM Trans. Graph.* 23, 3 (aug 2004), 796–803. <https://doi.org/10.1145/1015706.1015802>
- David Crandall, Andrew Owens, Noah Snavely, and Dan Huttenlocher. 2011. Discrete-continuous optimization for large-scale structure from motion. In *CVPR 2011*. IEEE, 3001–3008.
- Angela Dai, Angel X Chang, Manolis Savva, Maciej Halber, Thomas Funkhouser, and Matthias Nießner. 2017. Scannet: Richly-annotated 3d reconstructions of indoor scenes. In *Proceedings of the IEEE conference on computer vision and pattern recognition*. 5828–5839.
- Pinxuan Dai, Jiamin Xu, Wenxiang Xie, Xinguo Liu, Huamin Wang, and Weiwei Xu. 2024. High-quality Surface Reconstruction using Gaussian Surfels. In *SIGGRAPH 2024 Conference Papers*. Association for Computing Machinery. <https://doi.org/10.1145/3641519.3657441>
- Yuchao Dai, Zhidong Zhu, Zhibo Rao, and Bo Li. 2019. Mvs2: Deep unsupervised multi-view stereo with multi-view symmetry. In *2019 International Conference on 3D Vision (3DV)*. Ieee, 1–8.
- Kangle Deng, Andrew Liu, Jun-Yan Zhu, and Deva Ramanan. 2022. Depth-supervised NeRF: Fewer Views and Faster Training for Free. In *Proceedings of the IEEE/CVF Conference on Computer Vision and Pattern Recognition (CVPR)*.
- Daniel Duckworth, Peter Hedman, Christian Reiser, Peter Zhizhin, Jean-François Thibert, Mario Lučić, Richard Szeliski, and Jonathan T Barron. 2024. SMERF: Streamable memory efficient radiance fields for real-time large-scene exploration. *ACM Transactions on Graphics (TOG)* 43, 4 (2024), 1–13.
- Hugging Face. 2024. gsplat.js: JavaScript Gaussian Splatting library. <https://github.com/huggingface/gspat.js>. Accessed: 2024-05-15.
- Jan-Michael Frahm, Pierre Fite-Georgel, David Gallup, Tim Johnson, Rahul Raguram, Changchang Wu, Yi-Hung Jen, Enrique Dunn, Brian Clipp, Svetlana Lazebnik, et al. 2010. Building Rome on a cloudless day. In *Computer Vision—ECCV 2010: 11th European Conference on Computer Vision, Heraklion, Crete, Greece, September 5–11, 2010, Proceedings, Part IV 11*. Springer, 368–381.
- Linus Franke, Darius Rückert, Laura Fink, and Marc Stamminger. 2024. TRIPS: Trilinear Point Splatting for Real-Time Radiance Field Rendering. In *Computer Graphics Forum*. Wiley Online Library, e15012.
- Sara Fridovich-Keil, Alex Yu, Matthew Tancik, Qinhong Chen, Benjamin Recht, and Angjoo Kanazawa. 2022. Plenoxels: Radiance fields without neural networks. In *Proceedings of the IEEE/CVF Conference on Computer Vision and Pattern Recognition*. 5501–5510.
- Paul Furgale, Timothy D Barfoot, and Gabe Sibley. 2012. Continuous-time batch estimation using temporal basis functions. In *2012 IEEE International Conference on Robotics and Automation*. IEEE, 2088–2095.
- Paul Furgale, Joern Rehder, and Roland Siegwart. 2013. Unified temporal and spatial calibration for multi-sensor systems. In *2013 IEEE/RSJ International Conference on Intelligent Robots and Systems*. IEEE, 1280–1286.
- Yasutaka Furukawa, Brian Curless, Steven M. Seitz, and Richard Szeliski. 2010. Towards Internet-scale multi-view stereo. In *2010 IEEE Computer Society Conference on Computer Vision and Pattern Recognition*. 1434–1441. <https://doi.org/10.1109/CVPR.2010.5539802>
- Yasutaka Furukawa and Jean Ponce. 2010. Accurate, Dense, and Robust Multiview Stereo. *IEEE Transactions on Pattern Analysis and Machine Intelligence* 32, 8 (2010), 1362–1376. <https://doi.org/10.1109/TPAMI.2009.161>
- Michael Goesele, Noah Snavely, Brian Curless, Hugues Hoppe, and Steven M Seitz. 2007. Multi-view stereo for community photo collections. In *2007 IEEE 11th International Conference on Computer Vision*. IEEE, 1–8.
- Ian Goodfellow, Jean Pouget-Abadie, Mehdi Mirza, Bing Xu, David Warde-Farley, Sherjil Ozair, Aaron Courville, and Yoshua Bengio. 2014. Generative adversarial nets. *Advances in neural information processing systems* 27 (2014).
- Antoine Guédon and Vincent Lepetit. 2024. Sugar: Surface-aligned Gaussian Splatting for efficient 3d mesh reconstruction and high-quality mesh rendering. In *Proceedings of the IEEE/CVF Conference on Computer Vision and Pattern Recognition*. 5354–5363.
- Jared Heinly, Johannes L Schonberger, Enrique Dunn, and Jan-Michael Frahm. 2015. Reconstructing the world* in six days* (as captured by the yahoo 100 million image dataset). In *Proceedings of the IEEE conference on computer vision and pattern recognition*. 3287–3295.
- Baichuan Huang, Hongwei Yi, Can Huang, Yijia He, Jingbin Liu, and Xiao Liu. 2021. M3VSNNet: Unsupervised multi-metric multi-view stereo network. In *2021 IEEE International Conference on Image Processing (ICIP)*. IEEE, 3163–3167.
- Binbin Huang, Zehao Yu, Anpei Chen, Andreas Geiger, and Shenghua Gao. 2024. 2D Gaussian Splatting for Geometrically Accurate Radiance Fields. *SIGGRAPH* (2024).
- Yuheng Jiang, Zhehao Shen, Penghao Wang, Zhuo Su, Yu Hong, Yingliang Zhang, Jingyi Yu, and Lan Xu. 2024. Hifi4g: High-fidelity human performance rendering via compact Gaussian Splatting. In *Proceedings of the IEEE/CVF Conference on Computer Vision and Pattern Recognition*. 19734–19745.
- Michael Kazhdan, Matthew Bolitho, and Hugues Hoppe. 2006. Poisson surface reconstruction. In *Proceedings of the fourth Eurographics symposium on Geometry processing*, Vol. 7. 0.
- Nikhil Keetha, Jay Karhade, Krishna Murthy Jatavallabhula, Gengshan Yang, Sebastian Scherer, Deva Ramanan, and Jonathon Luiten. 2024. SplatTAM: Splat, Track & Map 3D Gaussians for Dense RGB-D SLAM. In *Proceedings of the IEEE/CVF Conference on Computer Vision and Pattern Recognition*.
- Bernhard Kerbl, Georgios Kopanas, Thomas Leimkühler, and George Drettakis. 2023. 3D Gaussian Splatting for Real-Time Radiance Field Rendering. *ACM Transactions on Graphics* 42, 4 (July 2023). <https://repo-sam.inria.fr/fungraph/3d-gaussian-splatting/>
- Bernhard Kerbl, Andreas Meuleman, Georgios Kopanas, Michael Wimmer, Alexandre Lanvin, and George Drettakis. 2024. A Hierarchical 3D Gaussian Representation for Real-Time Rendering of Very Large Datasets. *ACM Transactions on Graphics* 43, 4 (July 2024). <https://repo-sam.inria.fr/fungraph/hierarchical-3d-gaussians/>
- Justin Kerr, Chung Min Kim, Ken Goldberg, Angjoo Kanazawa, and Matthew Tancik. 2023. Lerf: Language embedded radiance fields. In *Proceedings of the IEEE/CVF International Conference on Computer Vision*. 19729–19739.
- Alexander Kirillov, Eric Mintun, Nikhila Ravi, Hanzi Mao, Chloe Rolland, Laura Gustafson, Tete Xiao, Spencer Whitehead, Alexander C. Berg, Wan-Yen Lo, Piotr Dollar, and Ross Girshick. 2023. Segment Anything. In *Proceedings of the IEEE/CVF International Conference on Computer Vision (ICCV)*. 4015–4026.
- Georgios Kopanas, Julien Philip, Thomas Leimkühler, and George Drettakis. 2021. Point-Based Neural Rendering with Per-View Optimization. In *Computer Graphics Forum*, Vol. 40. Wiley Online Library, 29–43.
- Jonas Kulhanek and Torsten Sattler. 2023. Tetra-nerf: Representing neural radiance fields using tetrahedra. In *Proceedings of the IEEE/CVF International Conference on Computer Vision*. 18458–18469.
- Kevin Kwok. 2023. splat. <https://github.com/antimatter15/splat>. Accessed: 2024-05-15.
- John J Leonard and Hugh F Durrant-Whyte. 1991. Simultaneous map building and localization for an autonomous mobile robot. In *IROS*, Vol. 3. 1442–1447.
- Jingliang Li, Zhengda Lu, Yiqun Wang, Ying Wang, and Jun Xiao. 2022. DS-MVNet: Unsupervised Multi-view Stereo via Depth Synthesis. In *Proceedings of the 30th ACM International Conference on Multimedia*. 5593–5601.
- Jinquan Li, Ling Pei, Danping Zou, Songpengcheng Xia, Qi Wu, Tao Li, Zhen Sun, and Wenxian Yu. 2020. Attention-SLAM: A visual monocular SLAM learning from human gaze. *IEEE Sensors Journal* 21, 5 (2020), 6408–6420.
- Jiahe Li, Jiawei Zhang, Xiao Bai, Jin Zheng, Xin Ning, Jun Zhou, and Lin Gu. 2024. DnGaussian: Optimizing sparse-view 3d Gaussian radiance fields with global-local depth normalization. In *Proceedings of the IEEE/CVF Conference on Computer Vision and Pattern Recognition*. 20775–20785.
- Zhuopeng Li, Lu Li, and Jianke Zhu. 2023. Read: Large-scale neural scene rendering for autonomous driving. In *Proceedings of the AAAI Conference on Artificial Intelligence*, Vol. 37. 1522–1529.
- Yiyi Liao, Jun Xie, and Andreas Geiger. 2022. KITTI-360: A novel dataset and benchmarks for urban scene understanding in 2d and 3d. *IEEE Transactions on Pattern Analysis and Machine Intelligence* 45, 3 (2022), 3292–3310.
- Chieh Hubert Lin, Hsin-Ying Lee, Willi Menapace, Menglei Chai, Aliaksandr Siarohin, Ming-Hsuan Yang, and Sergey Tulyakov. 2023. InfiniCity: Infinite-Scale City Synthesis. In *Proceedings of the IEEE/CVF international conference on computer vision*.
- Jiaqi Lin, Zhihao Li, Xiao Tang, Jianzhuang Liu, Shiyong Liu, Jiayue Liu, Yangdi Lu, Xiaofei Wu, Songcen Xu, Youliang Yan, and Wenming Yang. 2024. VastGaussian: Vast 3D Gaussians for Large Scene Reconstruction. In *CVPR*.
- Yang Liu, He Guan, Chuanchen Luo, Lue Fan, Junran Peng, and Zhaoxiang Zhang. 2024. CityGaussian: Real-time high-quality large-scale scene rendering with Gaussians. *arXiv preprint arXiv:2404.01133* (2024).
- Mulin Yu, Linning Xu, Yuanbo Xiangli, Limin Wang, Dahua Lin, Lu, Tao and Bo Dai. 2024. Scaffold-GS: Structured 3D Gaussians for View-Adaptive Rendering. *Conference on Computer Vision and Pattern Recognition (CVPR)* (2024).
- Hideobu Matsuki, Riku Murai, Paul H. J. Kelly, and Andrew J. Davison. 2024. Gaussian Splatting SLAM. (2024).
- Jérôme Maye, Paul Furgale, and Roland Siegwart. 2013. Self-supervised calibration for robotic systems. In *2013 IEEE Intelligent Vehicles Symposium (IV)*. IEEE, 473–480.
- Ben Mildenhall, Pratul P Srinivasan, Matthew Tancik, Jonathan T Barron, Ravi Ramamoorthi, and Ren Ng. 2021. Nerf: Representing scenes as neural radiance fields for view synthesis. *Commun. ACM* 65, 1 (2021), 99–106.
- Pierre Moulon, Pascal Monasse, and Renaud Marlet. 2013. Adaptive structure from motion with a contrario model estimation. In *Computer Vision—ACCV 2012: 11th Asian Conference on Computer Vision, Daejeon, Korea, November 5–9, 2012, Revised Selected Papers, Part IV 11*. Springer, 257–270.

- Thomas Müller, Alex Evans, Christoph Schied, and Alexander Keller. 2022. Instant neural graphics primitives with a multiresolution hash encoding. *ACM Transactions on Graphics (ToG)* 41, 4 (2022), 1–15.
- Simon Niedermayr, Josef Stumpfegger, and Rüdiger Westermann. 2024. Compressed 3d Gaussian splatting for accelerated novel view synthesis. In *Proceedings of the IEEE/CVF Conference on Computer Vision and Pattern Recognition*. 10349–10358.
- Atsuhiko Noguchi, Xiao Sun, Stephen Lin, and Tatsuya Harada. 2021. Neural articulated radiance field. In *Proceedings of the IEEE/CVF International Conference on Computer Vision*. 5762–5772.
- Luc Oth, Paul Furgale, Laurent Kneip, and Roland Siegwart. 2013. Rolling shutter camera calibration. In *Proceedings of the IEEE Conference on Computer Vision and Pattern Recognition*. 1360–1367.
- Federico Ponchio and Matteo Dellepiane. 2016. Multiresolution and fast decompression for optimal web-based rendering. *Graph. Model.* 88 (2016), 1–11. <https://api.semanticscholar.org/CorpusID:8770708>
- Daniel Rebain, Wei Jiang, Soroosh Yazdani, Ke Li, Kwang Moo Yi, and Andrea Tagliasacchi. 2021. Derf: Decomposed radiance fields. In *Proceedings of the IEEE/CVF Conference on Computer Vision and Pattern Recognition*. 14153–14161.
- Joern Rehder, Janosch Nikolic, Thomas Schneider, Timo Hinzmann, and Roland Siegwart. 2016. Extending kalibr: Calibrating the extrinsics of multiple IMUs and of individual axes. In *2016 IEEE International Conference on Robotics and Automation (ICRA)*. IEEE, 4304–4311.
- Konstantinos Rematas, Andrew Liu, Pratul P Srinivasan, Jonathan T Barron, Andrea Tagliasacchi, Thomas Funkhouser, and Vittorio Ferrari. 2022. Urban radiance fields. In *Proceedings of the IEEE/CVF Conference on Computer Vision and Pattern Recognition*. 12932–12942.
- Kerui Ren, Lihan Jiang, Tao Lu, Mulin Yu, Linning Xu, Zhangkai Ni, and Bo Dai. 2024. Octree-GS: Towards Consistent Real-time Rendering with LOD-Structured 3D Gaussians. *arXiv preprint arXiv:2403.17898* (2024).
- Barbara Roessle, Jonathan T. Barron, Ben Mildenhall, Pratul P. Srinivasan, and Matthias Nießner. 2022. Dense Depth Priors for Neural Radiance Fields from Sparse Input Views. In *Proceedings of the IEEE/CVF Conference on Computer Vision and Pattern Recognition (CVPR)*.
- Johannes Schauer and Andreas Nüchter. 2018. The peopleremover—removing dynamic objects from 3-d point cloud data by traversing a voxel occupancy grid. *IEEE robotics and automation letters* 3, 3 (2018), 1679–1686.
- Patrik Schumuck, Thomas Ziegler, Marco Karrer, Jonathan Perraudin, and Margarita Chli. 2021. Covins: Visual-inertial SLAM for centralized collaboration. In *2021 IEEE International Symposium on Mixed and Augmented Reality Adjunct (ISMAR-Adjunct)*. IEEE, 171–176.
- Markus Schütz et al. 2016. Potree: Rendering large point clouds in web browsers. *Technische Universität Wien, Wieden* (2016).
- Markus Schütz, Stefan Ohrhallinger, and Michael Wimmer. 2020. Fast Out-of-Core Octree Generation for Massive Point Clouds. In *Computer Graphics Forum*, Vol. 39. Wiley Online Library, 155–167.
- Johannes L Schönberger and Jan-Michael Frahm. 2016. Structure-from-motion revisited. In *Proceedings of the IEEE conference on computer vision and pattern recognition*. 4104–4113.
- Steven M Seitz, Brian Curless, James Diebel, Daniel Scharstein, and Richard Szeliski. 2006. A comparison and evaluation of multi-view stereo reconstruction algorithms. In *2006 IEEE computer society conference on computer vision and pattern recognition (CVPR'06)*, Vol. 1. IEEE, 519–528.
- Tixiao Shan, Brendan Englot, Carlo Ratti, and Daniela Rus. 2021. Lvi-sam: Tightly-coupled lidar-visual-inertial odometry via smoothing and mapping. In *2021 IEEE international conference on robotics and automation (ICRA)*. IEEE, 5692–5698.
- Qing Shuai, Haoyu Guo, Zhen Xu, Haotong Lin, Sida Peng, Hujun Bao, and Xiaowei Zhou. 2024. Real-Time View Synthesis for Large Scenes with Millions of Square Meters.
- Noah Snavely, Steven M Seitz, and Richard Szeliski. 2008. Skeletal graphs for efficient structure from motion. In *2008 IEEE Conference on Computer Vision and Pattern Recognition*. IEEE, 1–8.
- Cheng Sun, Min Sun, and Hwann-Tzong Chen. 2022. Direct Voxel Grid Optimization: Super-fast Convergence for Radiance Fields Reconstruction. In *CVPR*.
- Weiwei Sun, Eduard Trulls, Yang-Che Tseng, Sneha Sumbandam, Gopal Sharma, Andrea Tagliasacchi, and Kwang Moo Yi. 2023. PointNeRF++: A multi-scale, point-based Neural Radiance Field. *arXiv preprint arXiv:2312.02362* (2023).
- Chris Sweeney, Victor Frago, Tobias Höllerer, and Matthew Turk. 2016. Large scale sfm with the distributed camera model. In *2016 Fourth International Conference on 3D Vision (3DV)*. IEEE, 230–238.
- Matthew Tancik, Vincent Casser, Xinchen Yan, Sabeek Pradhan, Ben Mildenhall, Pratul P Srinivasan, Jonathan T Barron, and Henrik Kretzschmar. 2022. Block-nerf: Scalable large scene neural view synthesis. In *Proceedings of the IEEE/CVF Conference on Computer Vision and Pattern Recognition*. 8248–8258.
- Matthew Tancik, Ethan Weber, Evonne Ng, Ruilong Li, Brent Yi, Justin Kerr, Terrance Wang, Alexander Kristoffersen, Jake Austin, Kamyar Salahi, Abhik Ahuja, David McAllister, and Angjoo Kanazawa. 2023. Nerfstudio: A Modular Framework for Neural Radiance Field Development. In *ACM SIGGRAPH 2023 Conference Proceedings (SIGGRAPH '23)*.
- Jiaxiang Tang, Jiawei Ren, Hang Zhou, Ziwei Liu, and Gang Zeng. 2023. DreamGaussian: Generative Gaussian splatting for efficient 3d content creation. *arXiv preprint arXiv:2309.16653* (2023).
- Zachary Teed and Jia Deng. 2021. Droid-SLAM: Deep visual SLAM for monocular, stereo, and rgb-d cameras. *Advances in neural information processing systems* 34 (2021), 16558–16569.
- Haithem Turki, Deva Ramanan, and Mahadev Satyanarayanan. 2022. Mega-nerf: Scalable construction of large-scale nerfs for virtual fly-throughs. In *Proceedings of the IEEE/CVF Conference on Computer Vision and Pattern Recognition*. 12922–12931.
- Matias Turkulainen, Xuqian Ren, Iaroslav Melekhov, Otto Seiskari, Esa Rahtu, and Juho Kannala. 2024. DN-Splatter: Depth and Normal Priors for Gaussian Splatting and Meshing. *arXiv:2403.17822* [cs.CV]
- Peng Wang, Yuan Liu, Zhaoxi Chen, Lingjie Liu, Ziwei Liu, Taku Komura, Christian Theobalt, and Wenping Wang. 2023. F2-NeRF: Fast Neural Radiance Field Training with Free Camera Trajectories. In *Proceedings of the IEEE/CVF Conference on Computer Vision and Pattern Recognition*. 4150–4159.
- Changchang Wu. 2013. Towards linear-time incremental structure from motion. In *2013 International Conference on 3D Vision-3DV 2013*. IEEE, 127–134.
- Guanjun Wu, Taoran Yi, Jiemin Fang, Lingxi Xie, Xiaopeng Zhang, Wei Wei, Wenyu Liu, Qi Tian, and Xinggang Wang. 2024. 4d Gaussian Splatting for real-time dynamic scene rendering. In *Proceedings of the IEEE/CVF Conference on Computer Vision and Pattern Recognition*. 20310–20320.
- Xiuchao Wu, Jiamin Xu, Xin Zhang, Hujun Bao, Qixing Huang, Yujun Shen, James Tompkin, and Weiwei Xu. 2023. ScanNeRF: Scalable Bundle-Adjusting Neural Radiance Fields for Large-Scale Scene Rendering. *ACM Transactions on Graphics (TOG)* 42, 6 (2023), 1–18.
- Haozhe Xie, Zhaoxi Chen, Fangzhou Hong, and Ziwei Liu. 2024. Citydreamer: Compositional generative model of unbounded 3d cities. In *Proceedings of the IEEE/CVF Conference on Computer Vision and Pattern Recognition*. 9666–9675.
- Hongbin Xu, Zhipeng Zhou, Yu Qiao, Wenxiang Kang, and Qiuxia Wu. 2021a. Self-supervised multi-view stereo via effective co-segmentation and data-augmentation. In *Proceedings of the AAAI Conference on Artificial Intelligence*, Vol. 35. 3030–3038.
- Hongbin Xu, Zhipeng Zhou, Yali Wang, Wenxiang Kang, Baigui Sun, Hao Li, and Yu Qiao. 2021b. Digging into uncertainty in self-supervised multi-view stereo. In *Proceedings of the IEEE/CVF International Conference on Computer Vision*. 6078–6087.
- Qiangang Xu, Zexiang Xu, Julien Philip, Sai Bi, Zhixin Shu, Kalyan Sunkavalli, and Ulrich Neumann. 2022. Point-nerf: Point-based neural radiance fields. In *Proceedings of the IEEE/CVF Conference on Computer Vision and Pattern Recognition*. 5438–5448.
- Yunzhi Yan, Haotong Lin, Chenxu Zhou, Weijie Wang, Haiyang Sun, Kun Zhan, Xi-angpeng Lang, Xiaowei Zhou, and Sida Peng. 2024. Street Gaussians for Modeling Dynamic Urban Scenes. *arXiv:2401.01339* [cs.CV]
- Jiayu Yang, Jose M Alvarez, and Miaoimiao Liu. 2021. Self-supervised learning of depth inference for multi-view stereo. In *Proceedings of the IEEE/CVF Conference on Computer Vision and Pattern Recognition*. 7526–7534.
- Yao Yao, Zixin Luo, Shiwei Li, Tian Fang, and Long Quan. 2018. Mvsnet: Depth inference for unstructured multi-view stereo. In *Proceedings of the European conference on computer vision (ECCV)*. 767–783.
- Chandan Yeshwanth, Yueh-Cheng Liu, Matthias Nießner, and Angela Dai. 2023. ScanNet++: A high-fidelity dataset of 3d indoor scenes. In *Proceedings of the IEEE/CVF International Conference on Computer Vision*. 12–22.
- Alex Yu, Vickie Ye, Matthew Tancik, and Angjoo Kanazawa. 2021. pixelnerf: Neural radiance fields from one or few images. In *Proceedings of the IEEE/CVF Conference on Computer Vision and Pattern Recognition*. 4578–4587.
- Zehao Yu, Anpei Chen, Binbin Huang, Torsten Sattler, and Andreas Geiger. 2024. Mip-splatting: Alias-free 3d Gaussian Splatting. In *Proceedings of the IEEE/CVF Conference on Computer Vision and Pattern Recognition*. 19447–19456.
- Kai Zhang, Gernot Riegler, Noah Snavely, and Vladlen Koltun. 2020. Nerf++: Analyzing and improving neural radiance fields. *arXiv preprint arXiv:2010.07492* (2020).
- Richard Zhang, Phillip Isola, Alexei A Efros, Eli Shechtman, and Oliver Wang. 2018. The unreasonable effectiveness of deep features as a perceptual metric. In *Proceedings of the IEEE conference on computer vision and pattern recognition*. 586–595.
- Fuqiang Zhao, Yuheng Jiang, Kaixin Yao, Jiakai Zhang, Liao Wang, Haizhao Dai, Yuhui Zhong, Yingliang Zhang, Minye Wu, Lan Xu, et al. 2022a. Human performance modeling and rendering via neural animated mesh. *ACM Transactions on Graphics (TOG)* 41, 6 (2022), 1–17.
- Fuqiang Zhao, Wei Yang, Jiakai Zhang, Pei Lin, Yingliang Zhang, Jingyi Yu, and Lan Xu. 2022b. Humannerf: Efficiently generated human radiance field from sparse inputs. In *Proceedings of the IEEE/CVF Conference on Computer Vision and Pattern Recognition*. 7743–7753.
- Xiaoyu Zhou, Zhiwei Lin, Xiaojun Shan, Yongtao Wang, Deqing Sun, and Ming-Hsuan Yang. 2024. DrivingGaussian: Composite Gaussian Splatting for surrounding dynamic autonomous driving scenes. In *Proceedings of the IEEE/CVF Conference on Computer Vision and Pattern Recognition*. 21634–21643.

M. Zwicker, H. Pfister, J. van Baar, and M. Gross. 2001a. EWA volume splatting. In *Proceedings Visualization, 2001. VIS '01*. 29–538. <https://doi.org/10.1109/VISUAL.2001.964490>

Matthias Zwicker, Hanspeter Pfister, Jeroen Van Baar, and Markus Gross. 2001b. Surface splatting. In *Proceedings of the 28th annual conference on Computer graphics and interactive techniques*. 371–378.

A SPECIFICATIONS AND CALIBRATION OF POLAR DEVICE

Below, we provide the configuration and calibration details of our Polar scanner. The data acquisition unit comprises an Ouster OS0-128 REV6 LiDAR, an Insta360 ONE RS 1-inch 360 Edition Camera, and an Xsens MTi-630 IMU. Time synchronization across sensors is achieved using DEITY TC-1 timecode generators and simulated analog GPS NMEA time signals. The data collection unit and processing unit weigh 1250g and 850g, respectively, excluding the battery. The total apparatus weight does not exceed 3.2 kg, making it ideal for both handheld and wearable scanning applications. Additionally, we have engineered an over-shoulder support system to enhance operator stability during scans.

For the intrinsic parameter calibration of the fisheye camera and the IMU sensor, we leverage the program provided by OpenCV and the Allan Variance ROS toolbox [Furgale et al. 2012, 2013; Maye et al. 2013; Oth et al. 2013; Rehder et al. 2016], respectively. The extrinsic calibration between the fisheye camera and the IMU uses the Kalibr calibration program [Rehder et al. 2016]. Due to the sparsity, noisiness, and uncolored nature of the point cloud data collected by our LiDAR sensor, it is hard to establish correspondences between the LiDAR data and the images captured by the fisheye camera, making relative pose estimation between the sensors difficult. To address this issue, we introduce an additional sensor, a FARO laser scanner. This scanner provides dense, accurate, and colored point clouds and thus functions as a bridge for the relative pose estimation between the LiDAR sensor and the fisheye camera. Specifically, we adopt a checkerboard as our calibration scene and capture data from it using the FARO laser scanner and Polar device. The relative pose between the FARO laser scanner and the LiDAR sensor in our Polar device is achieved by point cloud registration, and that between the FARO laser scanner and the fisheye camera is obtained by establishing color correspondences between the point cloud captured by the FARO sensor and the fisheye image. By connecting the transformation from FARO to LiDAR and from FARO to the fisheye camera, we can finally calculate the extrinsic parameters between the LiDAR and the fisheye camera. We repeat this process twelve times in our implementation to reduce experimental error. It is important to note that FARO was only used to calibrate between the fisheye camera and the LiDAR **before** we start scanning a garage, and the process only needs to be conducted once.

B DATA PREPROCESSING AND MESH CLEANUP

To ensure data privacy, we anonymized vehicle license plate information recorded in the underground garage data collection. Specifically, we used image blurring to hide license plate numbers from identification. This step is essential to protect individual privacy and comply with data protection regulations. To remove the dynamic

objects in the collected data, we apply Segment Anything [Kirillov et al. 2023] to the images. For the point cloud data, we estimate whether the points scanned at one LiDAR frame are also observed at other frames, similar to Schauer and Nüchter[2018]. For mesh cleaning, we construct a kd-tree from the point cloud of LIV-SLAM and calculate the nearest neighbour distance of each mesh face ($k = 1$). If the distance exceeds 0.1 m, we remove the face.

C DETAILS OF DEPTH CALCULATION

To accurately calculate depth, we treat each Gaussian as a probability density function. Following [Zwicker et al. 2001a], we get the depth of each Gaussian primitive, d_i , by calculating the expected value of depth under this probability density as:

$$d_i = \frac{\int_{-\infty}^{+\infty} t g_i(\mathbf{x}) dx_2}{\int_{-\infty}^{+\infty} g_i(\mathbf{x}) dx_2} = \frac{1}{l} \frac{\int_{-\infty}^{+\infty} x_2 g_i(x_2 | x_0, x_1) dx_2}{\int_{-\infty}^{+\infty} g_i(x_2 | x_0, x_1) dx_2}, \quad (9)$$

where g_i is the Gaussian function, $\mathbf{x} = [x_0, x_1, x_2]^T$ is the coordinate of the space in the ray space, where x_0, x_1 are the pixel coordinates, x_2 is oriented in the same direction as the pixel ray. As in [Zwicker et al. 2001a], $t = x_2/l$ is the depth of \mathbf{x} in the camera coordinate system and $l = \sqrt{x_0^2 + x_1^2 + 1}$. We denote the center of the Gaussian in ray space as $\mathbf{p} = [p_0, p_1, p_2]$ and the covariance matrix as Σ , by defining $\mathbf{y} = \mathbf{x} - \mathbf{p}$, the Eqn. 9 can be simplified as:

$$\begin{aligned} d_i &= \frac{1}{l} \frac{\int_{-\infty}^{+\infty} (y_2 + p_2) g_i(\mathbf{y} + \mathbf{p}) dx_2}{\int_{-\infty}^{+\infty} g_i(\mathbf{y} + \mathbf{p}) dx_2} \\ &= \frac{1}{l} \left(p_2 + \frac{\int_{-\infty}^{+\infty} y_2 g_i(\mathbf{y} + \mathbf{p}) dy_2}{\int_{-\infty}^{+\infty} g_i(\mathbf{y} + \mathbf{p}) dy_2} \right). \end{aligned} \quad (10)$$

Then, $g(\mathbf{y} + \mathbf{p})$ can be expanded as:

$$g(\mathbf{y} + \mathbf{p}) = e^{-A y_2^2 + B y_2 + C} = e^C \cdot e^{-A y_2^2 + B y_2}, \quad (11)$$

where

$$\begin{aligned} A &= \frac{1}{2} (\Sigma^{-1})_{2,2} \\ B &= -(\Sigma^{-1})_{2,0} y_0 - (\Sigma^{-1})_{2,1} y_1 \\ C &= -\frac{1}{2} (\Sigma^{-1})_{0,0} y_0^2 - \frac{1}{2} (\Sigma^{-1})_{1,1} y_1^2 - (\Sigma^{-1})_{1,0} y_0 y_1 \end{aligned} \quad (12)$$

By integrating an arbitrary Gaussian function, we obtain:

$$\int_{-\infty}^{+\infty} e^{-A u^2 + B u} du = \sqrt{\frac{\pi}{A}} e^{\frac{B^2}{4A}}, \quad (13)$$

$$\int_{-\infty}^{+\infty} u e^{-A u^2 + B u} du = \frac{B}{2A} \sqrt{\frac{\pi}{A}} e^{\frac{B^2}{4A}}. \quad (14)$$

Next, substituting Eqn. 13 and Eqn. 14 into Eqn. 10 enables us to obtain:

$$d_i = \frac{1}{l} \left(p_2 + \frac{\int_{-\infty}^{+\infty} y_2 e^{-A y_2^2 + B y_2} dy_2}{\int_{-\infty}^{+\infty} e^{-A y_2^2 + B y_2} dy_2} \right) = \frac{1}{l} \left(p_2 + \frac{B}{2A} \right). \quad (15)$$

Finally, through simplification, Eqn. 15 can be transformed into Eqn. 4.

Before depth supervision, we normalize both the captured depth and predicted depth to $0 - 1$ as follows:

$$R(D) = \begin{cases} \frac{1}{2\beta}D & (D < \beta) \\ 1 - \frac{\beta}{2D} & (D \geq \beta) \end{cases}, \quad (16)$$

where $\beta = 10$, as the depth values within 10 meters are accurate. In this way, the same depth error results in a greater loss when closer to the camera than at further distances. It effectively avoids excessive depth loss for distant Gaussians due to inherently large depth values. This normalization also facilitates the storage of depth maps.